Atmos. Meas. Tech., 5, 1099–1119, 2012
www.atmos-meas-tech.net/5/1099/2012/
doi:10.5194/amt-5-1099-2012

Atmospheric Measurement Techniques

Retrieval of the optical depth and vertical distribution of particulate scatterers in the atmosphere using O_2 A- and B-band SCIAMACHY observations over Kanpur: a case study

S. Sanghavi[1], J. V. Martonchik[1], J. Landgraf[2], and U. Platt[3]

[1]Jet Propulsion Laboratory, California Institute of Technology, MS 169–237, 4800 Oak Grove Drive, Pasadena, CA 91109, USA
[2]Netherlands Institute of Space Research (SRON), Sorbonnelaan 2, 3584 CA Utrecht, The Netherlands
[3]Institute for Environmental Physics, Im Neuenheimer Feld 229, 69120 Heidelberg, Germany

Correspondence to: S. Sanghavi (suniti.sanghavi@gmail.com)

Received: 20 July 2011 – Published in Atmos. Meas. Tech. Discuss.: 8 November 2011
Revised: 23 April 2012 – Accepted: 27 April 2012 – Published: 16 May 2012

Abstract. Due to the well-defined vertical profile of O_2 in the atmosphere, the strong A-band (757–774 nm) has long been used to estimate vertical distributions of aerosol/cloud from space. We extend this approach to include part of the O_2 B-band (684–688 nm) as well. SCIAMACHY onboard ENVISAT is the first instrument to provide spectral data at moderate resolution (0.2–1.5 nm) in the UV/VIS/NIR including both the O_2 A- and B-bands. Using SCIAMACHY specifications, we make combined use of these bands in an optimal estimation algorithm. Theoretical studies show that our algorithm is applicable both over bright and dark surfaces for the retrieval of a lognormal approximation of the vertical profile of particulate matter, in addition to its optical thickness. Synthetic studies and information content analyses prove that such a combined use provides additional information on the vertical distribution of atmospheric scatterers, attributable to differences in the absorption strengths of the two bands and their underlying surface albedos.

Due to the high computational cost of the retrieval, we restrict application to real data to a case study over Kanpur through the year 2003. Comparison with AERONET data shows a commonly observed seasonal pattern of haziness, manifesting a correlation coefficient of $r = 0.92$ for non-monsoon monthly mean AOTs. The retrieved particulate optical thickness is found to be anti-correlated with the relative contrast of the Lambertian equivalent reflectivity (LER) at 682 nm and 755 nm by a coefficient of 0.788, confirming the hypothesis made in Sanghavi et al. (2010).

Our case study demonstrates a stable physics-based retrieval of particulate matter using only SCIAMACHY data. The feasibility of our approach is enhanced by the information provided by measurements around the O_2 B-band in addition to the A-band. Nonetheless, operational application to SCIAMACHY data remains challenged by radiometric uncertainties, yielding simultaneous retrieval of particle microphysical parameters impracticable and leading to over-reliance on climatological data. Addressing these issues in future instruments similar to SCIAMACHY, coupled with computational resources and speed-up of the current line-by-line radiative transfer calculations, can allow our approach to be extended to the global scale, particularly as it is not limited to dark surfaces.

1 Introduction

The vertical profiles of aerosol frequently provide a clear picture of transport processes, and are an indicator of elevated secondary aerosol formation or primary aerosol sources close to the surface. The vertical extent of clouds and aerosols also governs the sign and magnitude of their net radiative forcing. The importance of knowledge on the vertical distribution of aerosol is underlined by events such as the Eyjafjallajökull volcanic eruptions of April–May 2010, which caused a long and far-reaching disruption of air traffic. Less cataclysmic, but still of interest, are the everyday effects of

aerosol/cloud height in various areas ranging from public health (Yang et al., 2008; Pope III, 2000; Liu et al., 1991), climate prediction (Menon et al., 2002; Lohmann and Feichter, 1997; Charlson et al., 1992, 1991; Mitchell Jr., 1971), advective transport studies (Colarco et al., 2004; Balkanski et al., 1993), etc. From the perspective of remote sensing of trace gases, aerosols frequently impose severe uncertainties (Aben et al., 2007; Houweling et al., 2005; Boersma et al., 2004) that may be remedied by simultaneous, collocated knowledge of their vertical profile.

Lidar (Light Detection and Ranging) is an active remote sensing technique that measures the distance to an atmospheric scatterer as a function of the time taken for the emitted light pulse to be scattered back to the detector. Ground- and satellite-based lidar measurements presently provide excellent vertical information, but this is at the expense of limited spatial sampling. For example, CALIPSO flies over a given site only once every 16 days (1 daytime and 1 nighttime overpass) (Winker et al., 2003). Since aerosols and clouds induce large uncertainties in satellite retrievals of atmospheric trace gases from instruments such as SCIAMACHY, they would benefit most from information on the amount and vertical distribution of aerosol loading derived from the same sensor, i.e., collocated in space and time. This motivates the development of complementary methods to retrieve vertical information on aerosols using hyperspectral satellite data, typically used for trace gas retrievals. This also has the advantage of more frequent global coverage than lidar. As already suggested in previous work (Heidinger and Stephens, 2010; van Diedenhoven et al., 2007; Corradini and Cervino, 2006; Kokhanovsky and Rozanov, 2004; Rozanov and Kokhanovsky, 2004; Daniel et al., 2003; Koppers et al., 1997), the O_2 absorption bands contain information on the vertical structure of atmospheric scattering by virtue of the known vertical profile of atmospheric oxygen. The algorithm described here makes use of the O_2 A- and B- absorption bands, and can be adapted for correction of particulate scattering in any hyperspectral instrument containing the O_2 A-band and additional spectral proxies for vertical distribution like the O_2 B-band. In this work, we test our concept by means of synthetic studies and information content analyses, and subsequently apply it to SCIAMACHY (Bovensmann et al., 1999) measurements.

We present in the following a brief description of the SCIAMACHY instrument, whose measurements we have applied our retrieval concept to, followed by an outline of our retrieval algorithm in Sect. 3. This also includes a discussion of the behavior of the Jacobian matrix with respect to the retrieved parameters in Sect. 3.1 and an information content and error analysis in Sect. 3.2. We present a synthetic sensitivity study in Sect. 4 to test our retrieval concept, which we subsequently apply to real SCIAMACHY data over Kanpur in Sect. 5 before concluding this paper.

2 The SCIAMACHY instrument

The SCanning Imaging Absorption spectroMeter for Atmospheric CartograpHY (SCIAMACHY) instrument onboard Envisat flies around the Earth in a sun-synchronous polar orbit with a local equator crossing time of 10:30 a.m., recording the solar radiation transmitted, backscattered and reflected from the atmosphere at relatively high resolution (0.2 nm to 1.5 nm) over the range 240 nm to 1700 nm, and in selected regions between 2.0 µm and 2.4 µm. It has three different viewing modes, viz. nadir, limb, and sun/moon occultations. In the nadir viewing mode, which we use in this work, SCIAMACHY has a typical footprint of 30 km (along track) $\times$ 60 km (across track), achieving near-global coverage in 6 days. We focus in this work on the spectral ranges 755–775 nm and 684–688 nm, which contain the O_2 A- and B-bands, respectively, measured at a spectral resolution of $\approx$0.4 nm.

Longer term aerosol retrievals from SCIAMACHY have so far been limited to simple indices such as the Aerosol Absorbing Index (AAI) (de Graaf et al., 2007) or the SCattering Index (SCI) (Penning de Vries et al., 2009). Physics-based retrievals of optical thickness have been applied mainly to thick clouds. The application to aerosols includes a rigorous study of aerosol optical depth and vertical height retrievals (Kokhanovsky and Rozanov, 2010) applied to a dust cloud. However, this approach has not yet been extended to aerosols over a prolonged period of time. Synergistic approaches supported by climatological data have been successfully used to retrieve aerosol (Holzer-Popp et al., 2008) using SCIAMACHY data together with Advanced Along Track Scanning Radiometer (AATSR) data (Veefkind et al., 1999; Veefkind and de Leeuw, 1998).

This paper shows the feasibility of the physics-based retrievals of particulate optical thickness coupled with vertical information from satellites like SCIAMACHY, which can be applied stably over a longer period of time due to the additional information provided by measurements around the O_2 B-band. Nonetheless, application to SCIAMACHY data on an operational scale is severely challenged by radiometric uncertainties which make a simultaneous retrieval of aerosol microphysical parameters practically impossible, causing an over-reliance on climatological data which may be unavailable or unrepresentative for highly variable regimes. Addressing these issues in future instruments similar to SCIAMACHY, coupled with computational resources and speed-up of the current line-by-line radiative transfer calculations, can allow our approach to be extended to the global scale, taking advantage of the fact that it is not limited to dark surfaces.

3 Retrieval algorithm

In this section, we present our retrieval algorithm tailored to the requirements of the SCIAMACHY instrument, to which we apply our concept of combined usage of the O_2 A- and B-band spectral information. The general framework, however, can be applied to any instrument with similar capabilities, such as GOME-2 onboard MetOp (Callies et al., 2000).

A complete aerosol retrieval over a given location entails the determination of the microphysical parameters of the aerosol, including the complex refractive index and a possibly multimodal size distribution in addition to the aerosol optical thickness. Such retrievals are made by multi-angular and multi-spectral instruments like MISR (Diner et al., 1998) and multispectral instruments spanning the VIS, NIR, SWIR/MWIR and LWIR spectral regions like MODIS (Remer et al., 2005) on an operational level. More sophisticated approaches are being adopted to combine different instrumental capabilities with rigorous inversion methods (Dubovik et al., 2011). While SCIAMACHY supports many of the spectral channels to theoretically approach a MODIS-like retrieval, the inter-channel radiometric uncertainties and the large ground pixel size of SCIAMACHY are severe deterrents to such an endeavor.

Hence, for our retrieval, we are forced to make a climatology-based (Torres et al., 2007; Stammes and Noordhoek, 2002) assumption of the aerosol microphysical parameters, which fixes the aerosol extinction coefficients, the single scattering albedos and the phase function for the central wavelengths of both the O_2 A- and B-bands to be used in the forward model. These values are assumed to be constant throughout the band-width. For our synthetic sensitivity studies, and later for the case-study over Kanpur, we mostly assume the aerosol to be a relatively coarse urban absorbing type, IA3, having the microphysical parameters shown in Table 1. For some of the real-data retrievals, however, this assumption does not produce good retrievals, due to which we have had to make use of a finer, less absorbing urban aerosol type, IS1, to achieve a better fit with the observed measurements.

We determine the surface albedos for the two bands and their respective spectral gradients according to the time-series method demonstrated in Sanghavi et al. (2010). This involves the identification of clear-sky scenes from a measurement time series over a given satellite-observed ground pixel of unknown surface albedo and aerosol type. The lack of a general monotonic relationship between aerosol loading and observed reflectance, which generally encumbers the ordering of the observations according to aerosol loading, is ameliorated by using two wavelengths at which the surface albedos are known to differ. Treating each observation as cloud/aerosol free, we determine the corresponding Lambertian equivalent reflectance (LER), which has been referred to in Sanghavi et al. (2010) as apparent Lambertian equivalent albedo (ALEA). Denoting the LER's around the

Table 1. Aerosol microphysical parameters for a coarse, urban, absorbing aerosol (IA3). The bimodal number size distribution is calculated as

$$p_{\mathrm{aer}}(r)\,\mathrm{d}r = \frac{1}{\sqrt{2\pi}\,r}\left\{\frac{1-\rho_{\mathrm{mode}}}{\log\sigma_{\mathrm{f}}}\exp\left[-\frac{(\log r-\log r_{\mathrm{f}})^2}{2\,(\log\sigma_{\mathrm{f}})^2}\right]+\frac{\rho_{\mathrm{mode}}}{\log\sigma_{\mathrm{c}}}\exp\left[-\frac{(\log r-\log r_{\mathrm{c}})^2}{2\,(\log\sigma_{\mathrm{c}})^2}\right]\right\}\mathrm{d}r.$$

Refractive index, real component, n_{r}	1.45
Refractive index, imaginary component, n_{i}	0.012
Effective radius, fine mode, r_{f}	0.109 μm
Effective width, fine mode, σ_{f}	1.56
Effective radius, coarse mode, r_{c}	0.804 μm
Effective width, coarse mode, σ_{c}	2.004
Mode fraction of coarse mode, ρ_{mode}	6.95e-4

O_2 A- and B-bands by $\rho^{\mathrm{a}}_{\mathrm{A}}$ and $\rho^{\mathrm{a}}_{\mathrm{B}}$, their relative contrast $(\rho^{\mathrm{a}}_{\mathrm{A}}-\rho^{\mathrm{a}}_{\mathrm{B}})/(\rho^{\mathrm{a}}_{\mathrm{A}}+\rho^{\mathrm{a}}_{\mathrm{B}})$ decreases monotonically with increasing aerosol loading, with the clear-sky corresponding to the maximum value, when the true values are such that $\rho_{\mathrm{A}} > \rho_{\mathrm{B}}$. We use this technique to identify days of minimum aerosol loading in our time-series, which we treat as aerosol- and cloud-free for the estimation of the true surface albedos ρ_{A} and ρ_{B} around the O_2 A- and B-band, respectively.

We also assume a normalized lognormal vertical profile characterized by a peak height z_{p} and a peak width σ_{p} for the aerosol or cloud:

$$\rho_{\mathrm{aer}}(z)\,\mathrm{d}z = \frac{1}{\sqrt{2\pi}\,\sigma_{\mathrm{p}}z}\exp\left[-\frac{\left(\log z-\log z_{\mathrm{p}}\right)^2}{2\sigma_{\mathrm{p}}^2}\right]\mathrm{d}z, \quad (1)$$

where $\rho_{\mathrm{aer}}(z)\,\mathrm{d}z$ is the fraction of the total aerosol profile contained in an infinitesimal layer of geometrical thickness $\mathrm{d}z$ at a height z above the surface.

Since aerosols close to the surface are likely to have exponentially decreasing number concentrations, and since an exponential profile can be closely approximated by making $z_{\mathrm{p}} \to 0$, we consider the use of such a profile justified for aerosols occurring close to the ground. The other predominant scenario is the injection or production of aerosol at a finite height, e.g., by way of advection, a strong updraft, release from chimney stacks, or due to secondary aerosol formation, where a lognormal profile may be expected to form due to mixing in an atmosphere of exponentially falling density. We assume this to apply, albeit crudely, to clouds as well, letting geometrically thick or multilayered clouds be represented by larger values of σ_{p} than thin clouds. Multimodal distributions, however, are beyond the scope of this algorithm. We choose a priori values of $z_{\mathrm{p}} = 1.2$ km and $\sigma_{\mathrm{p}} = 0.85$ to approximate an exponentially decreasing profile with a scale height of 2 km, to conform with the generally expected profile of urban aerosols (Torres et al., 2007; Stammes

and Noordhoek, 2002). We find that this has practically no bearing on the retrieved values. Furthermore, we choose a low a priori AOT of 0.05 to prevent overshooting to negative values of AOT during intermediate retrieval iterations. In order to gain flexibility from the assumed model, we nominally include $\mathrm{d}\tau/\mathrm{d}\lambda$ in our state vector, with an a priori value laid down by our choice of aerosol model, and allow it to change in response to the observed scene by assigning it a variance of 10 % about this a priori value.

Using these assumptions and inputs, we seek to retrieve the aerosol optical depth τ_{700} at 700 nm and the vertical profile parameters z_p and σ_p by using optimal estimation to invert the logarithm of the reflectance measurements, $\ln R$, in the spectral ranges between 684–688 nm (O_2 B-band) and 757–774 nm (O_2 A-band). The reflectance at a given wavelength λ is defined as the ratio of the backscattered radiance $I(\lambda)$ with respect to the solar irradiance $I_0(\lambda)$ at the top-of-atmosphere, so that

$$R(\lambda) = \frac{I(\lambda)}{\mu_0\, I_0(\lambda)}, \tag{2}$$

where μ_0 is the cosine of the solar zenith angle. Thus, in optimization terminology, we have the following state vector $\boldsymbol{x}$ and measurement vector $\boldsymbol{y}$.

$$\boldsymbol{x} := \left\{\tau_{700},\, \frac{\mathrm{d}\tau}{\mathrm{d}\lambda},\, z_\mathrm{p},\, \sigma_\mathrm{p}\right\}, \tag{3}$$

and

$$\boldsymbol{y} := \{\ln R_\lambda\},\ \text{where}\ \lambda \in \{757\,\mathrm{nm},\, 774\,\mathrm{nm}\} \cap \{684\,\mathrm{nm},\, 688\,\mathrm{nm}\} \tag{4}$$

respectively.

We discard wavelengths beyond 688 nm in the B-band, because of the presence at these wavelengths of interfering lines of water absorption.

We choose the 700 nm wavelength for our AOT retrievals because it lies closely between the O_2 A- and B-bands as a result of which τ_{700} is less likely to propagate error due to any departure of the actual aerosol from the assumed aerosol type than, say, τ_{500} at the standard wavelength of 500 nm. For our assumed aerosol model (IA3), the optical thicknesses at the two wavelengths are related as follows:

$$\tau_{500} = 1.65 \cdot \tau_{700}, \tag{5}$$

which is large compared to the difference between τ_{700} and the optical thicknesses at the central wavelengths 686 nm and 765 nm, respectively:

$$\begin{aligned}\tau_{686} &= 1.03 \cdot \tau_{700}\\ \tau_{765} &= 0.87 \cdot \tau_{700}.\end{aligned} \tag{6}$$

The relationship between the measurement data, denoted by the measurement vector $\boldsymbol{y}$ and the set of parameters to be retrieved, denoted by the state vector $\boldsymbol{x}$, is given by

$$\boldsymbol{y} = F(\boldsymbol{x}) + \epsilon, \tag{7}$$

where ϵ is the retrieval error which combines measurement error and the error due to the forward model $F(\boldsymbol{x})$ used to approximate the physics of the measurement.

Optimal estimation (Rodgers, 2000) provides the following variation of the Gauss-Newton iterative scheme for the inversion of our state vector:

$$\begin{aligned}\boldsymbol{x}_{i+1} = \boldsymbol{x}_\mathrm{a} + \left(\mathbf{K}_i^T\, \mathbf{S}_\epsilon^{-1} \mathbf{K}_i + \mathbf{S}_\mathrm{a}^{-1}\right)^{-1} \mathbf{K}_i^T\\ \mathbf{S}_\epsilon^{-1}\left[\boldsymbol{y} - F\left(\boldsymbol{x}_i\right) + \mathbf{K}_i\left(\boldsymbol{x}_i - \boldsymbol{x}_\mathrm{a}\right)\right],\end{aligned} \tag{8}$$

where $\boldsymbol{x}_i$ and $\boldsymbol{x}_{i+1}$ are consecutive iterations of the state vector to be retrieved, $\boldsymbol{x}_\mathrm{a}$ is the a priori state vector obtained from climatology, $\mathbf{S}_\mathrm{a}$ is the a priori covariance matrix, $\mathbf{S}_\epsilon$ is the measurement covariance matrix, and $\mathbf{K}_i$ is the Jacobian of the forward model F calculated at $\boldsymbol{x}_i$.

The forward model $F(\boldsymbol{x})$ and the corresponding Jacobian $\mathbf{K}$ are computed using a linearized version of the Grant and Hunt Matrix Operator Method (GHMOM) radiative transfer model (Martonchik, 1975; Hunt and Grant, 1969). The HITRAN 2004 spectral database (Rothman et al., 2005) has been used to obtain the O_2 absorption cross-sections under the assumption of a Voigt line shape. Use has not been made of the updated HITRAN 2008 database (Rothman et al., 2009) that has since become available.

The iterations are assumed to have converged when the difference in the solutions obtained during consecutive iterations is smaller than the estimated error. Thus, our test for convergence is

$$\left(\boldsymbol{x}_i - \boldsymbol{x}_{i+1}\right)^T \mathbf{S}^{-1}\left(\boldsymbol{x}_i - \boldsymbol{x}_{i+1}\right) \lesssim 0.1\, N, \tag{9}$$

where N is the size of the state vector $\boldsymbol{x}$, and $\mathbf{S}$ is the a posteriori covariance matrix, given by

$$\mathbf{S} = \left(\mathbf{S}_\mathrm{a}^{-1} + \mathbf{K}_i^T\, \mathbf{S}_\epsilon^{-1} \mathbf{K}_i\right)^{-1}. \tag{10}$$

3.1 Jacobian matrix

The Jacobian matrix $\mathbf{K}$ is an $\boldsymbol{M} \times \boldsymbol{N}$ matrix, where $\boldsymbol{M}$ is the length of the measurement vector $\boldsymbol{y}$ and $\boldsymbol{N}$ is the length of the state vector $\boldsymbol{x}$, such that its elements consist of the derivative of the elements of forward model F (employed to simulate the measurement vector $\boldsymbol{y}$) with respect to the elements of $\mathbf{x}$, i.e.,

$$K_\mathrm{jk} = \frac{\partial F_\mathrm{j}}{\partial x_k},\quad \mathrm{j} \in 1, \ldots, M,\quad k \in 1, \ldots, N. \tag{11}$$

The Jacobian matrix is the main driver of the inverse solution and can provide rich insights into the physics of the

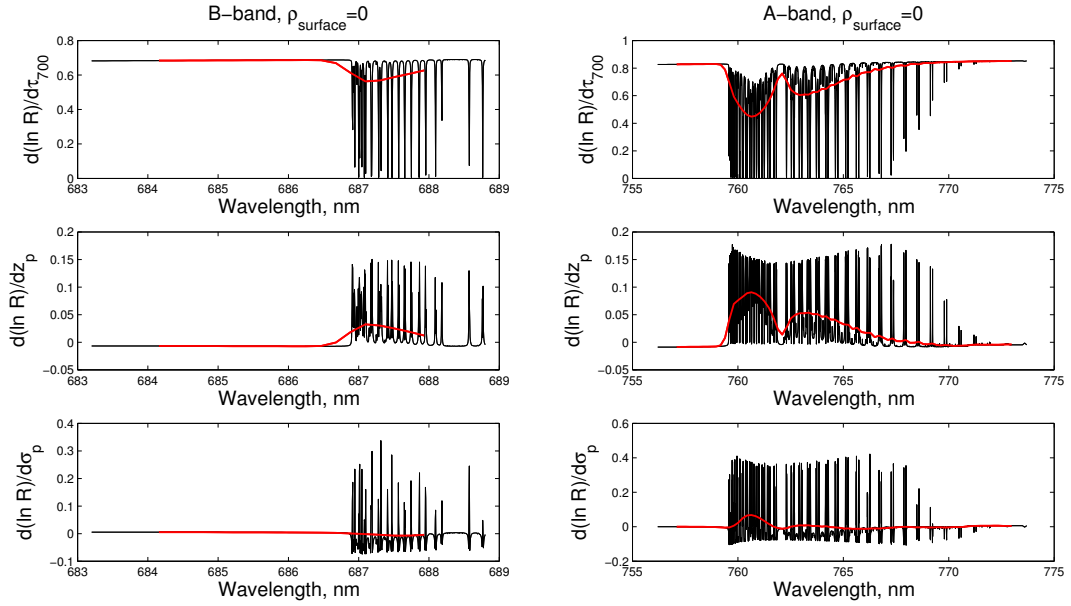

Fig. 1. A representation of the Jacobian matrix for a black surface. The spectra shown in black are computed at a fine resolution of 0.002 nm. The red curves are computed for the SCIAMACHY wavelength grid after convolution of the high resolution spectrum with a gaussian slit function having a FWHM of ≈0.4 nm. The top panels show the column of the Jacobian matrix corresponding to differentiation with respect to the aerosol optical thickness, τ_{700}. The middle and bottom panels represent derivatives with respect to the peak height z_p and the peak width σ_p, respectively. The Jacobians have been calculated at $\tau_{700} = 1.0$, $z_p = 3$ km and $\sigma_p = 0.7$ for a biomass aerosol. The viewing geometry is statistically representative for SCIAMACHY observations over Kanpur with SZA = 43°, LZA = 11°, Relative Azimuth = 149°. In each case, the left panel represents the B-band, while the right panel represents the A-band.

retrieval problem. Hence, before applying the above concept to synthetic and real retrievals, we present an inspection of the Jacobian of an arbitrarily chosen biomass aerosol (BL3) scenario having optical thickness $\tau_{700} = 1.0$, peak height, $z_p = 3$ km, and $\sigma_p = 0.7$ over three different surface conditions that will be revisited in the following sections, viz. a black surface, for which the albedos around both A- and B-bands, respectively ρ_A and ρ_B, are taken to be zero, a high contrast land surface, with $\rho_A \gg \rho_B$, typical of vegetation, and finally a medium contrast dark land surface, with $\rho_A \gtrsim \rho_B$, representative of sparsely vegetated surfaces. For the high contrast surface, we assume $\rho_A = 0.22$ and $\rho_B = 0.03$, for the medium contrast surface, we take $\rho_A = 0.13$ and $\rho_B = 0.09$.

In the following discussion, we define the "depth", Δ_R, of the logarithm of the radiance, $\ln R$, within the absorption lines relative to the logarithm of the radiance $\ln R_0$ in the continuum around it, so that

$$\Delta_R = \ln R_0 - \ln R. \tag{12}$$

(Our use of the logarithm of the reflectance instead of the reflectance alone is only motivated by the potential reduction of the non-linearity of the problem. It can be verified that this does not affect the results of the following discussion.)

From Eq. (12), we see that an increase in the absorption depth Δ_R due to a small change in a given aerosol parameter, x, manifests itself in lower values of the Jacobian, K, (a dip) at the absorption lines than the value of the Jacobian, K_0, in the continuum, while a decrease in the absorption depth is reflected in higher values of the Jacobian, K, (a bump) at the absorption lines relative to the value K_0 in the continuum. Formally, we can express this as

$$\frac{\partial(\Delta_R)}{\partial x} = \frac{\partial(\ln R_0 - \ln R)}{\partial x}, \tag{13}$$

so that

$$\text{for} \quad \frac{\partial(\Delta_R)}{\partial x} > 0, \quad \frac{\partial \ln R_0}{\partial x} > \frac{\partial \ln R}{\partial x} \implies K_0 > K, \tag{14}$$

and

$$\text{for} \quad \frac{\partial(\Delta_R)}{\partial x} < 0, \quad \frac{\partial \ln R_0}{\partial x} < \frac{\partial \ln R}{\partial x} \implies K_0 < K. \tag{15}$$

Before moving on to describe the Jacobians illustrated in Figs. 1, 2 and 3, it must be pointed out that the behavior of the Jacobians is specific to the state vector at which they are calculated. This is a consequence of the non-linearity of our problem. For example, the "depth", Δ_R, is seen to increase with increasing aerosol optical thickness in both bands for

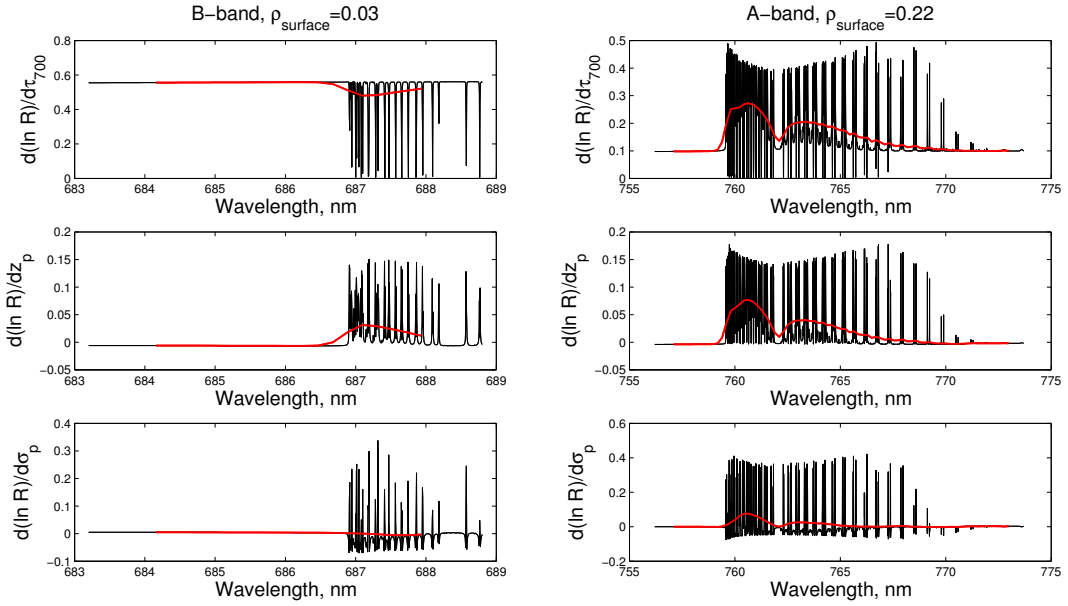

Fig. 2. Same as Fig. 1, but for a high contrast surface with $\rho_B = 0.03$ and $\rho_A = 0.22$. Note, however that the respective scales may differ.

the black surface. While we see in the following that this behavior varies with underlying surface albedo, it is not immediately apparent (but true) that it can also change if a different value of τ_{700} and/or z_p is chosen.

Figure 1 represents the black surface, where the top panels show the column of the Jacobian matrix corresponding to differentiation with respect to the aerosol optical thickness, τ_{700}. The middle and bottom panels represent derivatives with respect to the peak height z_p and the peak width σ_p, respectively. In each case, the left and right panels represent the B-band and the A-band, respectively. The spectra shown in black have been computed at a fine resolution of 0.002 nm. The red curves have been computed for the SCIAMACHY wavelength grid after convolution of the high resolution spectrum with the corresponding instrumental slit function (assumed to be gaussian with a FWHM of $\approx$0.4 nm).

In the top panels of Fig. 1, we notice that the respective depths, $\Delta_{R,A}$ and $\Delta_{R,B}$, of both the A- and B-bands increase with increasing aerosol optical thickness. This is a direct consequence of the longer geometrical path of light arriving at the detector after undergoing increased multiple scattering due to aerosol, which causes the absorbing wavelengths to suffer more extinction relative to the non-absorbing parts of the spectrum.

The middle and bottom panels, on the other hand, suggest a decrease in the band depths, $\Delta_{R,A}$ and $\Delta_{R,B}$, with increasing z_p and σ_p. An increase in the peak height z_p causes more light to be scattered back without traversing the more absorbing lower layers of the atmosphere. Also to be noted is that the amount of multiple scattering is amplified by the number of ambient Rayleigh scatterers. Since more Rayleigh scatterers reside closer to the surface, less multiple scattering occurs at higher altitudes (for unsaturated absorption lines), further shortening the mean optical light path.

The decrease in band depths, $\Delta_{R,A}$ and $\Delta_{R,B}$, with respect to σ_p is much weaker than that due to z_p, to the extent that there is nearly no discernible change in the B-band. This is because an increase in σ_p merely results in a symmetrical redistribution of the aerosol towards the log normal tails of the vertical distribution function. Strong absorption lines are more sensitive to higher atmospheric levels, since they are already saturated before they reach the lower layers. Weak lines, on the other hand, show less bias in their vertical sensitivity since the atmosphere remains transparent at those wavelengths up to greater depths. This is reflected in the relatively large decrease in the geometric depths of the strong absorption lines, resulting in a decrease in the A-band depth, while the depth of B-band remains nearly unchanged.

We now examine Fig. 2 representing the high contrast surface and notice that, contrary to the black surface, the depth of the A-band, $\Delta_{R,A}$, decreases with respect to aerosol optical thickness. In this case, higher aerosol optical thickness causes a "shielding effect" which prevents photons from traversing the lower atmosphere to reach the bright surface, thereby decreasing the optical path length, leading to less absorption. The behavior with respect to z_p and σ_p, however, remains practically unchanged, since they do not have any impact on the net shielding effect of the aerosol.

Figure 3 represents the dark, medium contrast surface in which the top left and right panels suggest that the depth of the B-band, $\Delta_{R,B}$, sees a slight increase and that of the A-band, $\Delta_{R,A}$, experiences as slight decrease with increasing aerosol optical thickness. In each of these cases, the surface

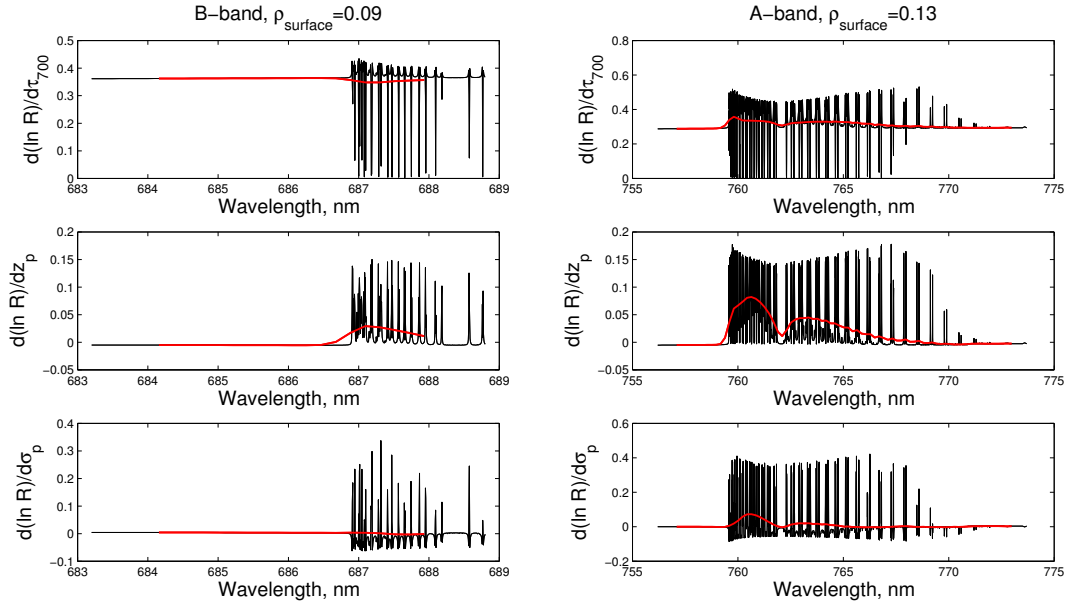

Fig. 3. Same as Fig. 1, but for a dark, medium contrast surface with $\rho_B = 0.09$ and $\rho_A = 0.13$. Note, however that the respective scales may differ.

is bright enough to be eclipsed by the shielding effect of aerosols resulting in a decrease in optical light path. However, the aerosols can also cause a sufficient increase in multiple scattering to eventually "outshine" the underlying surface and increase the optical light path. These opposing effects compete with each other in this case, with the former being slightly stronger in the A-band and the latter dominating slightly in the B-band. Again, the behavior with respect to z_p and σ_p remains nearly unchanged, suggesting that the dependence of the measurement on the vertical profile is not greatly affected by the surface albedo.

The patterns discussed above are also evident in Fig. 4, which shows a direct comparison of Jacobian columns after convolution with the SCIAMACHY slit function for all surface types, the black, green and red curves representing the black, high contrast and dark medium contrast surfaces, respectively, revealing the strong influence of the underlying surface albedo on the behavior of the reflectance with respect to changes in aerosol optical thickness. Here we have not extended our discussion to the competing effects of the viewing geometry. Given a Lambertian surface, we can easily infer that a more slanting viewing geometry increases the atmospheric light path, so that the aerosol effect on the reflectance becomes increasingly dominant, eventually exceeding the surface effect for the surfaces considered here. A discussion on the competing effects of surface and aerosol within the A-band, taking into account the viewing geometry can be found in van Diedenhoven et al. (2005).

3.2 Information content and error analysis

The Jacobian matrix, $\mathbf{K}$, coupled with the measurement error covariance matrix $\mathbf{S}_\epsilon$, and the a priori covariance matrix $\mathbf{S}_a$, respectively representing the uncertainty associated with the measured reflectances and with the inverted parameters before the measurement is made, provide a host of diagnostic tools (Rodgers, 2000) with which we can estimate the information content of our retrieval and the error in the retrieved parameters due to various sources. The sources of error that we are interested in are mainly those due to:

1. variation in $\frac{d\tau}{d\lambda}$ due to departure of the true aerosol type from the assumed one,
2. variation in the true surface albedos, from their assumed values, ρ_A and ρ_B, and
3. model bias due to an incorrect representation of the observed scene or measurement bias due to errors in the absolute radiometric calibration of the instrument, which is expected in the case of SCIAMACHY to be of the order of 10–20 % (Kokhanovsky et al., 2008; Acarreta and Stammes, 2005) around the A- and B-bands, but are ameliorated by use of appropriate correction factors (van Diedenhoven et al., 2005; Noël, 2004).

The a posteriori covariance matrix, $\mathbf{S}_x$, gives the uncertainty (or error) associated with the state vector after the measurement is made. $\mathbf{S}_x$ can be calculated using simply $\mathbf{K}$, $\mathbf{S}_\epsilon$ and $\mathbf{S}_a$ as

$$\mathbf{S}_x = \left[\mathbf{K}^T \mathbf{S}_\epsilon^{-1} \mathbf{K} + \mathbf{S}_a^{-1}\right]^{-1}. \quad (16)$$

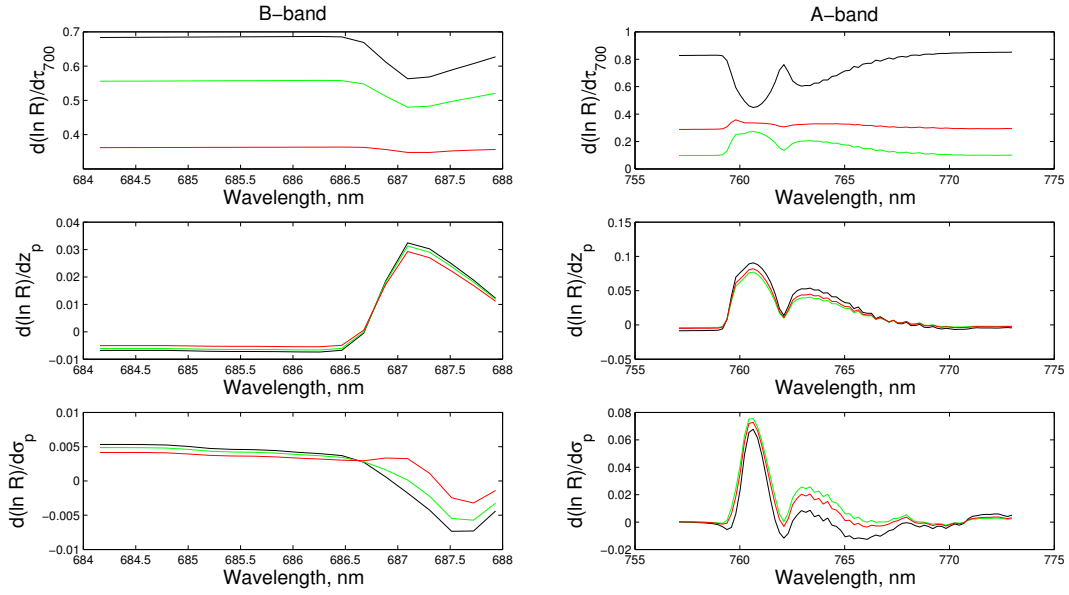

Fig. 4. Convolved Jacobian matrix representations for the black surface (black curve), high contrast surface (green curve), dark medium contrast surface (red curve). The top, middle and bottom panels show derivatives with respect to optical thickness τ_{700}, peak height z_p and peak width σ_p, respectively.

For SCIAMACHY measurements, we may assume the radiometric noise to be better than 1 % of the measurement, so that for a measurement vector consisting of reflectances, R, the measurement covariance matrix is a diagonal matrix whose diagonal terms are given by

$$\mathbf{S}_{\epsilon,ij} = \delta_{ij}\,(0.01 \cdot R_i)^2, \tag{17}$$

where $\delta_{\mathrm{ij}} = 1$ for $i = j$ and $\delta_{ij} = 0$ for $i \neq j$. The off-diagonal covariance terms are negligible for SCIAMACHY measurements.

(In this section, we have taken a measurement vector composed of simply reflectances, R, and not the logarithm of the reflectances, ln R as in the rest of this paper. This has only been done for the sake of simplicity of demonstration and does not have a noteworthy effect on the results discussed in this section. Also, the state vector has been expanded to include the surface albedos in the two bands, ρ_A and ρ_B, respectively.)

For our analysis, we consider an ideal a priori covariance matrix with diagonal terms given by the squares of the natural ranges of variation of the respective parameters τ_{700}, $\frac{\mathrm{d}\tau}{\mathrm{d}\lambda}$, z_p, σ_p, ρ_A and ρ_B in the absence of any prior knowledge about them, so that

$$\mathbf{S}_{\mathrm{a},ij}^{\frac{1}{2}} := \delta_{ij}\,\frac{1}{\sqrt{2}}\left\{10,\, 4.16 \times 10^{-3} \times \tau,\, 15,\, 5,\, 1,\, 1\right\}, \tag{18}$$

where we roughly allow τ_{700} to vary between 0–10, the range for $\frac{\mathrm{d}\tau}{\mathrm{d}\lambda}$ is obtained from an assumed variation of the Ångström exponent between -1 and 2, z_p may vary between 0–15 km, σ_p varies between 0 and 5, and the surface albedos may take any value between 0 and 1. This is the covariance matrix that would allow all variables practically unrestricted freedom in their respective natural ranges.

However, when we fix a given parameter, it is equivalent to expecting very low uncertainty in its a priori value. Hence, we also consider such a constrained a priori covariance matrix, $\mathbf{Cu}_\mathrm{a}$, in which we constrain the values of $\frac{\mathrm{d}\tau}{\mathrm{d}\lambda}$, ρ_A and ρ_B to vary within 10 % of their a priori values, so that

$$\mathbf{Cu}_{\mathrm{a},ij}^{\frac{1}{2}} := \delta_{ij}\,\frac{1}{\sqrt{2}}\left\{10,\, 0.1 \cdot \left(\frac{\mathrm{d}\tau}{\mathrm{d}\lambda}\right)_\mathrm{a},\, 15,\, 5,\, 0.1 \cdot \rho_\mathrm{A},\, 0.1 \cdot \rho_\mathrm{B}\right\}. \tag{19}$$

We notice that the uncertainties allowed in Eq. (19) for z_p and σ_p are unrealistically large, which can cause instabilities in our retrieval. Hence, we further constrain the retrieval by limiting the assumed uncertainties in the vertical distribution parameters such that we get an a priori covariance matrix that effectively damps z_p and σ_p:

$$\mathbf{Cd}_{\mathrm{a},ij}^{\frac{1}{2}} := \delta_{ij}\,\frac{1}{\sqrt{2}}\left\{10,\, 0.1 \cdot \left(\frac{\mathrm{d}\tau}{\mathrm{d}\lambda}\right)_\mathrm{a},\, 1,\, 0.5,\, 0.1 \cdot \rho_\mathrm{A},\, 0.1 \cdot \rho_\mathrm{B}\right\}. \tag{20}$$

This time, our constraints are not strong enough to fix the corresponding parameters, but sufficient for preventing changes in parameters that are so large that the retrieval algorithm becomes unstable. In this case, the constraints play more the role of a "damping factor", similar to that used in regularization methods (Tikhonov, 1963; Phillips, 1962) or in the Levenberg-Marquardt method (Levenberg, 1944; Marquardt, 1963). This is the a priori covariance matrix we use in our synthetic retrievals and the retrievals made for the case-study over Kanpur.

Table 2. Information content per parameter retrieved for different retrieval set-ups. The number of retrieved parameters vary from 3 for the two constrained cases, 5 for the unconstrained cases involving only the A- or the B-band, and 6 for the unconstrained cases using both the A- and B-band.

Surface	Information content (A + B)			Information content (A-only)			Information content (B-only)		
	constr. 2	constr. 1	unconstr.	constr. 2	constr. 1	unconstr.	constr. 2	constr. 1	unconstr.
Black	7.30	9.23	7.52	5.87	7.77	6.52	4.49	5.62	4.20
Medium contrast	6.96	8.10	5.96	5.20	6.12	4.92	3.88	4.57	3.41
High contrast	6.77	8.21	5.77	4.98	5.30	4.40	4.21	5.19	3.84

The ratio of the a priori and the a posteriori covariance matrices provide a measure of the information gained due to the measurement, as reflected by the information content, H, (Rodgers, 2000; Weaver, 1949; Shannon, 1948) of the measurement defined as

$$H = \frac{1}{2} \ln_2 \left| \mathbf{S}_x^{-1} \mathbf{S}_\mathrm{a} \right|. \quad (21)$$

This is a useful quantity that we use in the following to compare the information gained by the combined use of both the A- and B-bands compared to that of one band alone.

To assess the error introduced in the retrieval of one parameter of the state vector due to an error in the retrieved/assumed value of another, we use the averaging kernel matrix, **A**, which provides the sensitivity of the retrieval to the true state of the atmosphere-surface system. It is defined as

$$\mathbf{A} = \frac{\partial \boldsymbol{x}}{\partial \boldsymbol{x}^*} = \left[\mathbf{K}^T \mathbf{S}_\epsilon^{-1} \mathbf{K} + \mathbf{S}_\mathrm{a}^{-1} \right]^{-1} \mathbf{K}^T \mathbf{S}_\epsilon^{-1} \mathbf{K}, \quad (22)$$

where $\boldsymbol{x}$ and $\boldsymbol{x}^*$ represent the retrieved and true state vectors.

The averaging kernel matrix can also be written as

$$\mathbf{A} = \mathbf{G}\mathbf{K}, \quad (23)$$

where $\mathbf{G} = \frac{\partial \boldsymbol{x}}{\partial \boldsymbol{y}}$ is the gain matrix that provides the sensitivity of the retrieval to the measurement, $\boldsymbol{y}$ (or the error in it). The gain matrix, **G**, is defined formally as

$$\mathbf{G} = \left[\mathbf{K}^T \mathbf{S}_\epsilon^{-1} \mathbf{K} + \mathbf{S}_\mathrm{a}^{-1} \right]^{-1} \mathbf{K}^T \mathbf{S}_\epsilon^{-1}. \quad (24)$$

We use the gain matrix in the following to estimate the error due to measurement bias in each of the retrieved parameters.

We examine the quantities introduced above for an aerosol of the type we assume over Kanpur (IA3) at an optical thickness of 0.5 and for the three different surfaces introduced earlier, viz. a black surface having respective albedos $\rho_\mathrm{A} = 0$ and $\rho_\mathrm{B} = 0$ in the O_2 A- and B-bands, a medium contrast surface with $\rho_\mathrm{A} = 0.13$ and $\rho_\mathrm{B} = 0.09$, and a high contrast surface with $\rho_\mathrm{A} = 0.22$ and $\rho_\mathrm{B} = 0.03$. Our choice of aerosol type sets $\frac{\mathrm{d}\tau}{\mathrm{d}\lambda} = -2.15 \times 10^{-4}\,\mathrm{nm}^{-1}$, $z_\mathrm{p} = 1.2\,\mathrm{km}$ and $\sigma_\mathrm{p} = 0.85$. The constrained cases have

1. the $\frac{\mathrm{d}\tau}{\mathrm{d}\lambda}$, ρ_A and ρ_B values fixed within 10 % of their assumed a priori values, according to the a priori covariance matrix $\mathbf{C}\mathbf{u}_\mathrm{a}$ defined in Eq. (19), and
2. the $\frac{\mathrm{d}\tau}{\mathrm{d}\lambda}$, ρ_A and ρ_B values fixed within 10 % of their assumed a priori values, with additional damping for parameters z_p and σ_p according to the a priori covariance matrix $\mathbf{C}\mathbf{d}_\mathrm{a}$ defined in Eq. (20).

The unconstrained cases are free to vary within their natural ranges as in Eq. (18).

Table 2 shows the information content (obtained according to Eq. 21) of the retrieval per retrieved parameter for both the damped and undamped constrained as well as unconstrained cases for each of the three surfaces considered in the previous sections (black, medium contrast and high contrast) when use is made of both the O_2 A- and B-bands, only the A-band or only the B-band, respectively. It is immediately clear that the use of both the O_2 A- and B-bands significantly enhances the information content of the retrieval compared to using only the A- or B-band. This applies uniformly to all levels of surface contrast and brightness, irrespective of whether the retrieval is constrained or not.

Going down the tabulated values of information content for A-only and B-only retrievals in Table 2, we notice that the information content always decreases with increasing surface brightness. This, however, ceases to apply for the combined A- and B-band retrievals, where, even though the black surface has the maximum information content, the non-black surfaces have very similar values, with the high contrast surface surpassing the one with medium contrast for constrained retrievals, even though the A-band brightness of the high contrast case (0.22) is considerably higher than for the medium contrast case (0.13).

Comparing the undamped constrained and unconstrained cases, we observe across all surface types and for combined as well as individual use of the A- and B-bands, that significantly more information is retrieved per parameter, when parameters that can be known a priori with a high degree of confidence are constrained. We sacrifice some information content in damped constrained retrievals, but still remain above the information content level of unconstrained retrievals. To see how the information content of a retrieval translates into the accuracy of retrieval of the individual parameters, we have tabulated the a posteriori standard deviations expected in the retrieved parameters for each of the three surfaces and retrieval set-ups in Table 3. We see for the aerosol optical thickness retrievals, that applying constraints

Table 3. Accuracy of retrieval for each retrieved parameter for different retrieval set-ups (obtained from a posteriori variances).

Surface	Parameter	Retrieval uncertainty (A + B)			Retrieval uncertainty (A-only)			Retrieval uncertainty (B-only)		
		constr. d	constr. u	unconstr.	constr. d	constr. u	unconstr.	constr. d	constr. u	unconstr.
Black	τ_{700}	±0.008	±0.009	±0.11	±0.011	±0.012	±0.13	±0.013	±0.013	±0.37
	$\frac{d\tau}{d\lambda}$ [nm^{-1}]	(±0.00002)	(±0.00002)	±0.00008	(±0.00002)	(±0.00002)	±0.00008	(±0.00002)	(±0.00002)	±0.0010
	z_p [km]	±0.28	±0.55	±2.29	±0.32	±0.60	±2.85	±0.53	±1.47	±7.03
	σ_p	±0.31	±0.81	±0.95	±0.32	±0.84	±0.95	±0.35	±3.45	±3.53
	ρ_A	(±0.0015)	(±0.0016)	±0.021	(±0.002)	(±0.002)	±0.025	(±0.002)	(±0.002)	±0.707
	ρ_B	(±0.0015)	(±0.0015)	±0.019	(±0.002)	(±0.002)	±0.707	(±0.002)	(±0.002)	±0.064
Medium contrast	τ_{700}	±0.035	±0.078	±0.23	±0.037	±0.122	±0.25	±0.084	±0.102	±0.58
	$\frac{d\tau}{d\lambda}$ [nm^{-1}]	(±0.00002)	(±0.00002)	±0.0004	(±0.00002)	(±0.00002)	±0.0004	(±0.00002)	(±0.00002)	±0.0014
	z_p [km]	±0.65	±1.90	±3.94	±0.68	±2.57	±4.53	±0.68	±2.78	±8.74
	σ_p	±0.35	±1.984	±2.55	±0.35	±2.16	±2.56	±0.35	±3.49	±3.53
	ρ_A	(±0.004)	(±0.010)	±0.030	(±0.005)	(±0.015)	±0.033	(±0.018)	(±0.018)	±0.707
	ρ_B	(±0.005)	(±0.010)	±0.030	(±0.013)	(±0.013)	±0.707	(±0.011)	(±0.013)	±0.075
High contrast	τ_{700}	± 0.024	±0.03	±0.21	±0.047	±0.20	±0.24	±0.026	±0.03	±0.44
	$\frac{d\tau}{d\lambda}$ [nm^{-1}]	(±0.00002)	(±0.00002)	±0.0007	(±0.00002)	(±0.00002)	±0.0008	(±0.00002)	(±0.00002)	±0.0012
	z_p [km]	±0.49	±1.56	±3.47	± 0.69	±3.37	±3.67	±0.61	±1.75	±7.94
	σ_p	±0.34	±1.88	±2.11	±0.35	±3.09	±3.24	±0.35	±3.48	±3.53
	ρ_A	(±0.002)	(±0.002)	±0.017	(±0.004)	(±0.016)	±0.019	(±0.031)	(±0.031)	±0.707
	ρ_B	(±0.004)	(±0.004)	±0.033	(±0.004)	(±0.004)	±0.707	(±0.004)	(±0.004)	±0.060

on well-known parameters, especially the surface albedos, improves retrieval accuracy by almost an order of magnitude in all cases. This is expected because of the very similar effects of aerosol optical thickness and surface albedo on the observed signal, making it difficult to distinguish between them. Thus, application of constraints improves the retrieval of aerosol optical thickness at $\tau_{700} = 0.5$ for A + B retrievals by reducing the error from about 20 % to less than 2 % of the true value.

For a black surface, the retrieval error in $\frac{d\tau}{d\lambda}$ is sufficiently small in both the constrained and unconstrained cases for all retrieval set-ups other than B-only retrievals, so that the application of strong constraints is not necessary. However, for brighter surfaces, the lack of constraints makes the retrieval unstable. Nevertheless, slightly loosening the constraints we have applied on $\frac{d\tau}{d\lambda}$ from 10 % to about $20-30$% may improve the accuracy and speed of our retrievals in the future.

For z_p and σ_p, it can be seen that both the A- and B-bands are required with damped constraints for a reliable retrieval. The retrieval of the vertical distribution parameters works better for darker surfaces. A higher contrast between the A- and B-bands also contributes to improving the accuracy of the retrieval. An effect that is not apparent from Table 3 is that the parameters z_p and σ_p exhibit a strong negative covariance with each other, offsetting mutual retrieval errors.

It is clear from Table 3 that we expect to know the surface albedo values ρ_A and ρ_B to a 10 times better accuracy in the constrained cases than without any previous knowledge about it. In the subsequent discussion, we present an analysis of the errors that would be introduced into the retrieved parameters due to error in our estimation of such "fixed" quantities

The above discussion explored the inherent accuracy of the general retrieval, under the assumption that all input parameters were accurately known. We now proceed to discuss the main errors introduced by external sources, including errors in our assumption of "fixed" parameters $\frac{d\tau}{d\lambda}$ and the surface reflectances ρ_A and ρ_B, as well as due to measurement or forward model biases.

3.2.1 Error due to variation in $\frac{d\tau}{d\lambda}$ due to departure of the true aerosol type from the assumed type

The main types of particulate scatterers that may prevail over Kanpur include urban pollution aerosol, smoke, desert dust and water cloud, of which urban pollution may be regarded as the most predominant. The maximum deviation that we can expect in the value of $\frac{d\tau}{d\lambda}$ is between urban pollution ($\frac{d\tau}{d\lambda} = -2.155 \times 10^{-4}\,\mathrm{nm}^{-1}$) and water cloud ($\frac{d\tau}{d\lambda} = -1.706 \times 10^{-5}\,\mathrm{nm}^{-1}$), so that the maximum error in its estimation is about $\Delta\frac{d\tau}{d\lambda} = 2 \times 10^{-4}\,\mathrm{nm}^{-1}$. No mixing between different aerosol types has been considered here. Given this value, we use the averaging kernel matrix defined in Eq. (22) to estimate the maximum error in other retrieved parameters due to $\Delta\frac{d\tau}{d\lambda}$ for combined A- and B-band retrievals, as shown in Table 4. Even though there are variations between the different levels of constraint, we notice that the errors remain small enough so as not to affect the overall stability of the retrieval.

3.2.2 Error due to variation in the true surface albedos from their assumed values, ρ_A and ρ_B

Using the method outlined in Sanghavi et al. (2010), we obtain 4 days during the year 2003 over Kanpur that qualify as clear sky days. The mean and standard deviation of the surface albedos at Kanpur are found to be 0.201 ± 0.023 around the O_2 A-band and 0.063 ± 0.006 around the O_2 B-band.

Table 4. Errors caused in the retrieval of other retrieved parameters at the maximum deviation of $\frac{d\tau}{d\lambda}$ from its assumed value.

Surface	Parameter	Smoothing error due to $\Delta\frac{d\tau}{d\lambda} = 2 \times 10^{-4}$		
		constr. d	constr. u	unconstr.
Black	τ_{700}	4×10^{-4}	0.0046	-4×10^{-4}
	z_p [km]	0.055	−0.046	0.008
	σ_p	0.042	0.213	0.002
Medium contrast	τ_{700}	0.0078	-5.1×10^{-4}	− 0.0018
	z_p [km]	0.028	0.058	0.031
	σ_p	0.010	0.209	0.025
High contrast	τ_{700}	6×10^{-4}	−0.0024	-3×10^{-4}
	z_p [km]	0.108	0.075	0.013
	σ_p	0.027	0.186	0.042

Given the location of Kanpur in the Indian subcontinent with no deciduous vegetation or likelihood of snowfall, we can expect the only cause of change in albedo to be an increase at wavelengths beyond ≈700 nm during/after the rainy season (June–September) due to a possible increase in foliage. However, the 4 clear sky days mentioned above include one in early October, which does not show any marked difference compared to the other three days which are in the months of February and March. There may, however, be a systematic overestimation of surface albedo due to contamination from background aerosol. Assuming this to account for 100 % of the lowest albedo retrieved, we roughly arrive at a maximum error of $\Delta\rho_A = \Delta\rho_B = 0.063$. Using this value, we again use the averaging kernel matrix defined in Eq. (22) to estimate the maximum error in other retrieved parameters due to $\Delta\rho_A$ and $\Delta\rho_B$ for combined A- and B-band retrievals, as shown in Table 5.

For every surface, an increase in actual surface albedo effectively leads to a retrieval of higher aerosol optical thickness. As would be intuitively expected, the increase in AOT is negligibly small when the surface albedo is unconstrained, but becomes sizable when the surface albedo is fixed. Also, a higher than assumed surface albedo leads to underestimation of z_p and σ_p as the aerosol is now required to mimic scattering due to the surface at the bottom of the atmosphere (more pronouncedly in the constrained cases).

3.2.3 Error due to instrumental measurement bias

SCIAMACHY underestimates the reflectance in the visible range by 10–20 % (Acarreta and Stammes, 2005), which is remedied by the use of correction factors as described in van Diedenhoven et al. (2005) and Noël (2004). Use has been made in our case-study of SCIAMACHY V5 data which the authors have found to provide better vertical parameter retrievals than the subsequently radiometrically corrected SCIAMACHY V6 data.

We do not delve into modeling errors due to surface pressure, since we expect them to be marginally small (1–2 hPa) compared to other sources of uncertainty in our retrieval problem. We include in our forward model calculations the surface pressure predicted by ECMWF over Kanpur at the time of each SCIAMACHY overpass, which we expect to reliably limit surface pressure error (Salstein et al., 2008). We also use altimetric data to correct for small changes in surface altitude, which are likewise unlikely to cause substantial error in our case, given the relatively flat terrain around Kanpur.

Also, potential interferences with chlorophyll fluorescence (Guanter et al., 2010) are currently ignored but could be evaluated using the same methodology described above.

We have excluded the single scattering albedo, ω, of the aerosol from our state vector, opting instead to "fix" it to the value dictated by climatology (occasionally changing the assumed aerosol type to achieve a better fit with measurements over Kanpur). This is because we expect to see considerable anti-covariance between the AOT and ω, making it difficult to separate their effects. However, we notice that the error introduced by the assumption of an absorbing aerosol like Type IA3 ($\omega = 0.89$) when the true aerosol is closer to a more scattering type like IS1 ($\omega = 0.95$), can cause large error due to wrong representation of the measured scenario (upto 50 %), depending on the aerosol optical thickness and viewing geometry. We have attempted to ameliorate such errors in our case-study retrievals by occasional use of other aerosol types, mainly IS1, when our principal assumption of the IA3 aerosol type fails to achieve an acceptable convergence. Uncertainties in the single scattering albedo have not been accounted for in our sensitivity study, since our main aim in this paper has been to demonstrate the vertical information contained in the A- and B-bands. However, it would be very interesting to explore this in the future, preferably by supplementing the current measurement vector with measurements made at a larger number of wavelengths that are spaced spectrally farther from each other. The current application to SCIAMACHY does not allow for this approach, due to strong channel-to-channel radiometric irregularities.

Given an arbitrarily chosen bias of 6 % in both bands after radiometric correction, the gain matrix defined in Eq. (24) enables the calculation of the corresponding errors expected in the retrieved parameters as shown in Table 6.

As we would expect, an overestimation of the TOA reflectance signal leads to a corresponding overestimation of the aerosol optical thickness in the constrained albedo cases. When the albedo is left unconstrained, the surface albedo is overestimated and the aerosol optical thickness is underestimated. The effect of bias on the absorption lines is more complex, leading to different responses from z_p and σ_p depending upon the surface and the applied constraints.

Table 5. Errors caused in the retrieval of other retrieved parameters at the maximum deviation of ρ_A and ρ_B from their assumed values.

Surface	Parameter	Smoothing error due to $\Delta\rho_A = 0.063$			Smoothing error due to $\Delta\rho_B = 0.063$		
		constr. d	constr. u	unconstr.	constr. d	constr. u	unconstr.
Black	τ_{700}	0.153	0.163	2.5×10^{-4}	0.165	0.177	2.8×10^{-4}
	z_p [km]	−3.17	−3.42	−0.0052	−3.43	−3.63	−0.0059
	σ_p	−0.514	−0.615	−0.0012	−0.579	−0.804	−0.0013
medium contrast	τ_{700}	0.055	0.278	8.8×10^{-4}	0.030	0.152	8.8×10^{-4}
	z_p [km]	−0.887	−4.37	−0.0139	−0.485	−2.37	−0.0139
	σ_p	−0.174	−1.836	−0.0062	−0.096	−1.032	−0.0064
High contrast	τ_{700}	0.289	0.385	8.4×10^{-4}	0.003	0.004	4.2×10^{-4}
	z_p [km]	−3.572	−5.863	−0.0128	−0.035	−0.047	−0.0065
	σ_p	−0.706	−1.342	−0.0029	−0.007	−0.027	−0.0018

Table 6. Errors caused in the retrieval of retrieved parameters due to a measurement bias of 6 % (arbitrarily chosen).

Surface	Parameter	Error due to a measurement bias of 6 %		
		constr. d	constr. u	unconstr.
Black	τ_{700}	0.022	0.019	−0.053
	z_p [km]	0.765	0.607	2.123
	σ_p	0.193	0.572	0.979
Medium contrast	τ_{700}	0.072	0.067	−0.029
	z_p [km]	0.061	0.602	2.131
	σ_p	−0.057	−0.456	0.310
High contrast	τ_{700}	0.054	0.038	−0.014
	z_p [km]	0.61	1.40	2.21
	σ_p	0.102	−0.305	0.018

4 Sensitivity studies

The analysis of Sect. 3.2 has been presented on the basis of only one point in state space. In view of the non-linearity of our retrieval problem, a more detailed analysis covering more states (i.e., different values of τ_{700}, $\frac{d\tau}{d\lambda}$, z_p, σ_p, ρ_A, ρ_B) is needed for a representative depiction. This, however, is beyond the scope of this paper. The sensitivity studies described in this section cover a range of τ_{700}, z_p, and σ_p that is wide enough to showcase the general behavior of our retrieval set-up.

In order to test the robustness of the retrieval concept outlined in Sect. 3, we carried out sensitivity studies using synthetic SCIAMACHY data generated at different aerosol optical thicknesses and different lognormal vertical distributions, under the same three surface conditions presented in Sect. 3.1, viz. a black surface, where both ρ_A and ρ_B were taken to be zero, a high contrast land surface, with $\rho_A \gg \rho_B$, typical of vegetation, and a medium contrast land surface, with $\rho_A \gtrsim \rho_B$, representative of sparsely vegetated surfaces. The viewing geometry was chosen to be statistically representative for SCIAMACHY observations over Kanpur with a solar zenith angle (SZA) of $\theta_0 = 43°$, a line-of-sight zenith angle (LZA) of $\theta = 11°$, and a relative azimuth of $\phi = 149°$.

Varying the aerosol optical thickness at 700 nm, denoted in this section as $\tau_{aerosol}$, in each case between 0.05–2.0, the peak height, z_p, between 1–7 km, and the peak width, σ_p, between 0.5–1.0, under a measurement error given by a random noise of 1 % of the measured reflectance, we compare the retrieved quantities to their true values.

In Fig. 5, the red asterisks show the retrieved aerosol optical thicknesses plotted against their true values, which are nearly coincident with the black 1:1 line. The retrieval of vertical parameters is not exact at lower values of $\tau_{aerosol}$, as is apparent from the offset between the blue (for z_p) and magenta (for σ_p) circles from their respective true values. This is to be expected, since at low aerosol optical thicknesses, the vertical distribution has a negligible contribution to the measurement, as a result of which the vertical profile parameters are more constrained by their a priori values ($z_p = 1.2$ km and $\sigma_p = 0.85$) than by the measurement. This situation is most apparent in the high contrast case, where increased multiple scattering due to the high surface albedo around the A-band causes more blurring of information on the vertical profile. Almost paradoxically however, the retrieval over the black surface is not as good as that over the dark medium contrast surface, highlighting that the difference in surface albedos in the A- and B-bands adds to the information content of the latter measurement. This is also true of the retrieval of the vertical profile parameters, z_p and σ_p, as shown in Figs. 6 and 7, respectively. In Fig. 6, the red asterisks represent the retrieved peak height, z_p, plotted against its true value. The blue and magenta circles represent the retrieved values of $\tau_{aerosol}$ and σ_p, respectively, shown against their respective true values. Again, the alignment of the asterisks along the black 1:1 line indicate the good retrievability of the peak height. This is less true of σ_p as shown by Fig. 7. These retrievals are expected to improve with increasing z_p, due to the greater sensitivity of the A-band at higher altitudes. At $z_p = 2$ km, though, only the moderate contrast surface shows

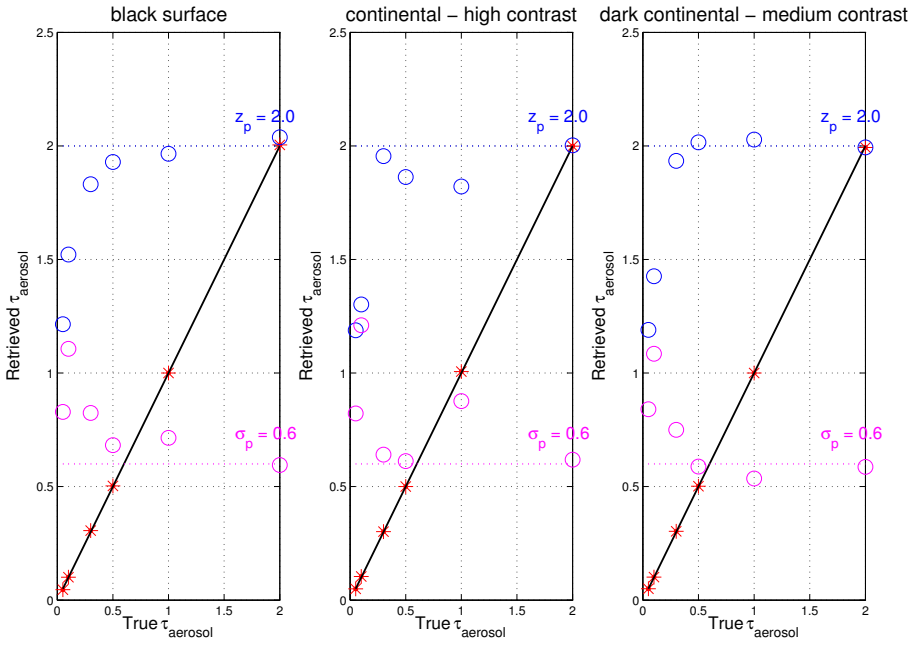

Fig. 5. Synthetic retrievals of aerosol optical thickness τ_{aerosol} (red asterisks), peak height z_{p} (blue circles) and peak width σ_{p} (magenta circles), for varying τ_{aerosol} and fixed parameters $z_{\text{p}} = 2$ km (blue dashed line) and $\sigma_{\text{p}} = 0.6$ (magenta dashed line). The black line is the 1:1 line. A coarse urban absorbing aerosol (IA3) has been used. The viewing geometry is statistically representative for SCIAMACHY observations over Kanpur with SZA = 43°, LZA = 11°, Azimuth = 149°. Left panel: black surface, $\rho_{\text{A}} = \rho_{\text{B}} = 0$, middle panel: land surface having high contrast, $\rho_{\text{A}} = 0.22$, $\rho_{\text{B}} = 0.03$, right panel: dark land surface having medium contrast, $\rho_{\text{A}} = 0.13$, $\rho_{\text{B}} = 0.09$.

a satisfactory retrieval. In the other two instances, the red asterisks representing the retrieved values of σ_{p} are seen to depart considerably from the black 1:1 lines. We see an overestimation of low σ_{p} in the high contrast case, which is likely to be a result of blurring due to increased multiple scattering around the O_2 A-band, due to the high reflectivity of the surface. Also, in the case of the high contrast surface and the black surface, there occurs a loss of information at large σ_{p}, as a result of which the a priori constraints dominate the retrieval causing an underestimation of the retrieved σ_{p}. The retrieved values also reflect an anti-correlation between the deviation from the truth of z_{p} and σ_{p}, as can be seen from the corresponding departure of the magenta circles representing z_{p} from its true value. The blue circles representing τ_{aerosol}, however, are still well-aligned with their true value.

In summary, we can assume robust retrievability for τ_{aerosol} and good retrievability for the peak height, z_{p}, of log-normal vertical distributions, but relatively limited information on σ_{p}, depending on the brightness and contrast of the underlying surface. The surface reflectances around the two bands and the differences thereof play an important role in determining how well posed the inversion problem is. Low surface reflectances reduce the amount of multiple scattering and hence allow more visibility through the vertical column, whereas the difference between the surface albedos adds to the constraints present in the inversion problem, thus improving its information content. Consequently, the combined use of the O_2 A- and B-bands allows good retrievals also over brighter surfaces, provided there is sufficient contrast between the albedos in the two bands.

We test this hypothesis in the following section over the city of Kanpur, located in a semi-arid region in the Indo-gangetic plains, over the year 2003, following the drought of 2002 (Kripalani et al., 2004). While the sensitivity studies dealt with a known aerosol type, a homogeneous surface and a clearly defined lognormal profile, these assumptions become only crude approximations of the real scene observed by SCIAMACHY. Our choice of Kanpur for the case-study is motivated by an attempt to minimize such difficulties of representation.

5 Retrievals over Kanpur, India, using SCIAMACHY data

The application of our inversion method to SCIAMACHY data requires some limitations to be borne in mind. Uncertainties in radiometric calibration can lead to biases in the retrieval and the large footprint (30 km × 60 km) of the instrument frequently makes a homogenous forward model representation of the observed scene implausible, not only in terms of cloud cover but also surface albedo. The resulting departure from truth, combined with that due to forward model assumptions with regard to aerosol microphysical properties and surface type, can limit the representability of the scene

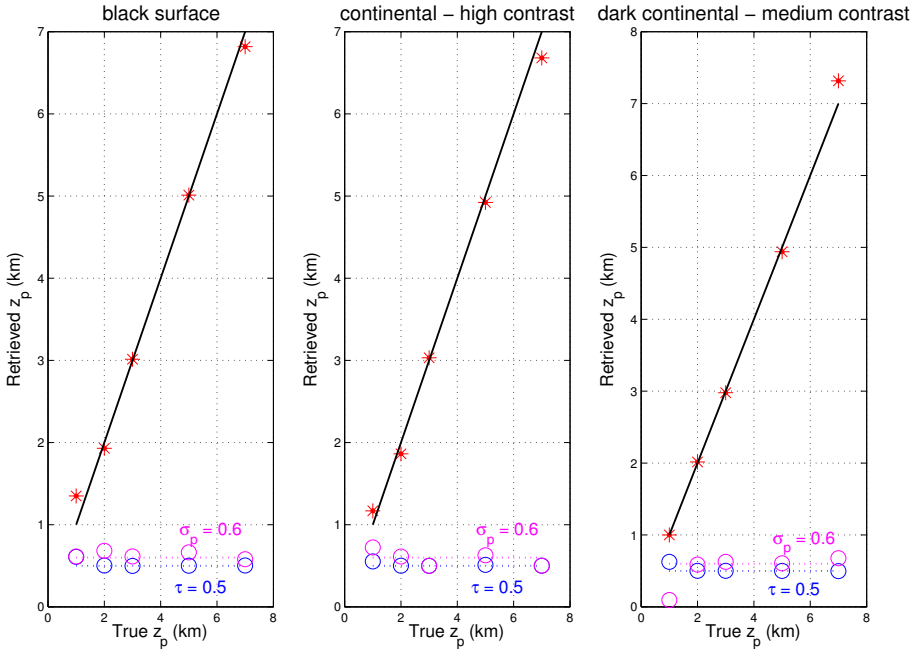

Fig. 6. Synthetic retrievals of the peak height of a lognormal aerosol vertical profile z_p (red asterisks), aerosol optical thickness $\tau_{aerosol}$ (blue circles) and peak width σ_p (magenta circles), for varying z_p and fixed parameters $\tau_{aerosol} = 0.5$ (blue dashed line) and $\sigma_p = 0.6$ (magenta dashed line). The black line is the 1:1 line. A coarse urban absorbing aerosol (IA3) has been used. The viewing geometry is statistically representative for SCIAMACHY observations over Kanpur with SZA = 43°, LZA = 11°, Azimuth = 149°. Left panel: black surface, $\rho_A = \rho_B = 0$, middle panel: land surface having high contrast, $\rho_A = 0.22$, $\rho_B = 0.03$, right panel: dark land surface having medium contrast, $\rho_A = 0.13$, $\rho_B = 0.09$.

being observed, consequently affecting the accuracy of the inversion.

Radiometric calibration issues around the O_2 A- and B-bands are not very severe and are more easily alleviated by co-retrieving the correction factors under tight constraints, so as not to undermine the retrieval of aerosol parameters. However, we have to rely almost entirely on climatology for information on aerosol type, since we do not have the sensitivity to track changes in the microphysical properties of the aerosol. In order to ameliorate resulting errors in our case-study retrievals, we have to make occasional use of other aerosol types, typically IS1, when our principal climatological assumption of the IA3 aerosol type fails to achieve an acceptable convergence.

Due to computational constraints, we have restricted the application of our algorithm to SCIAMACHY data obtained over Kanpur, India, during the year 2003. Located in the Indo-gangetic plains, this is an area of considerable interest for studies of aerosol. It hosts an AERONET site that we use to validate our results. Predominantly due to the tropical location of Kanpur, the surface albedo does not display much seasonality on account of the absence of large-scale changes in vegetation or snow cover, as a result of which the surface albedo can be assumed to be constant throughout the year. The subtropical, non-coastal location of Kanpur also increases the probability of cloudless scenes and, thus, the number of measurements that truly qualify as hazy without clouds. However, given the large size of the SCIAMACHY pixel, we do not attempt to filter out clouds in favor of retrieving only aerosols, or vice versa. Our motivation is to make maximum use of all measurements by attempting to find an effective representation of the particulate matter present in a given scene. Consequently, we retrieve more clouds than aerosols in the monsoon season (mid-June through September), while retrievals at other times of the year are dominated by haze.

Since the microphysical aspect of particulate scattering is only involved in our study through the single scattering albedo ω, the phase function $p(\theta)$ and the spectral dependence of the AOT, $\frac{d\tau}{d\lambda}$, the representation of clouds by assuming a scattering aerosol of type IS1, though not perfect, is acceptable at low cloud fraction, especially due to the similarity of the single scattering albedo ω, the flexibility in the value of the retrieved quantity $\frac{d\tau}{d\lambda}$, and the fact that differences in the phase function do not hamper measurements made in a single viewing angle geometry. In view of the fact, however, that such a representation of the phase function can lead to over-estimation of cloud optical thickness, we do not include retrieved optical thicknesses beyond $\tau_{700} = 4$ in our analysis, since they are likely to represent high cloud fraction

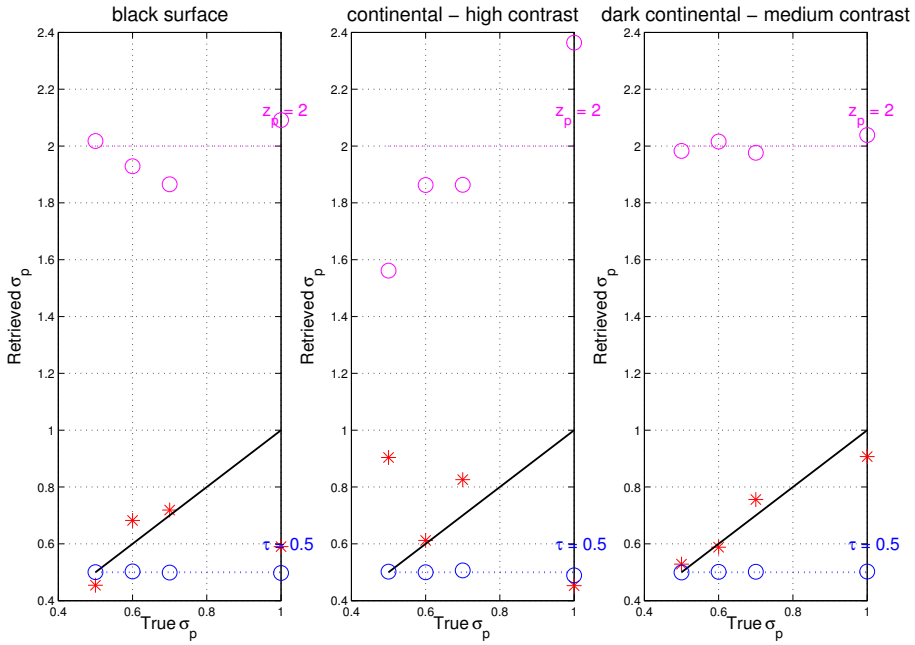

Fig. 7. Synthetic retrievals of the peak width of a lognormal aerosol vertical profile σ_p (red asterisks), aerosol optical thickness $\tau_{aerosol}$ (blue circles) and peak height z_p (magenta circles), for varying σ_p and fixed parameters $\tau_{aerosol} = 0.5$ (blue dashed line) and $z_p = 2$ km (magenta dashed line). The black line is the 1:1 line. A coarse urban absorbing aerosol (IA3) has been used. The viewing geometry is statistically representative for SCIAMACHY observations over Kanpur with SZA = 43°, LZA = 11°, Azimuth = 149°. Left panel: black surface, $\rho_A = \rho_B = 0$, middle anel: land surface having high contrast, $\rho_A = 0.22$, $\rho_B = 0.03$, right panel: dark land surface having medium contrast, $\rho_A = 0.13$, $\rho_B = 0.09$.

scenarios. We do include, however, the vertical information retrieved, since this is relatively unaffected by errors in phase function/optical thickness.

We have analyzed SCIAMACHY measurements obtained during 51 overpasses in 2003 over Kanpur. Based on the method of maximum relative contrast (Sanghavi et al., 2010), we assigned a clear sky scene to 7 March 2003, corresponding to a surface albedo $\rho_A = 0.21$ and $\rho_B = 0.07$ around the A- and B-bands, respectively. Our method calculates the Lambertian equivalent reflectivities (LER, referred to as ALEA in Sanghavi et al., 2010), ρ_A and ρ_B, at two different absorption-free wavelengths, one near the A-band at 755 nm, and the other near the B-band at 682 nm, respectively. Using these LER's, we compute the "relative contrast" of a given scene as $(\rho_A - \rho_B)/(\rho_A + \rho_B)$. For a given geometry, the relative contrast is found to decrease monotonically with increasing aerosol loading. Building a time series of the relative contrasts of all measurements available over a given location, we assign a clear sky scene to the one with maximum relative contrast, enabling the determination of the surface albedo (assumed Lambertian).

Choosing coarse absorbing aerosol microphysics typical of the region (Torres et al., 2007; Stammes and Noordhoek, 2002) for our forward model, we applied the above inversion to the measurements after correcting them radiometrically using the correction factors recommended in van Diedenhoven et al. (2005) and Noël (2004). It is clear that forward model error cannot be completely eliminated in the case of real retrievals as in a synthetic sensitivity study. A quantitative analysis of retrieval errors caused by error in ground pixel representation through uncertainties in surface albedos for instruments like GOME (Burrows et al., 1999) and SCIAMACHY is provided by van Diedenhoven et al. (2007), indicating that errors due to representation of a given scene can far exceed the measurement error of the instrument.

To deal with such limitations which prevent normal convergence, we iterate our retrieval for a total of $N_{max} = 12$ times, computing the least squares mean of the resultant fit for each iteration, and choose the result of the iteration that produces the smallest least square mean value. In most cases of low AOT and very high AOT, the retrieval converges in significantly less than the 12 iterations. This may be attributable to the better representability of such scenes due to increased homogeneity. Other scenes (usually corresponding to intermediate values of AOT) produce different solutions corresponding to comparable least squares fits, undermining the confidence with which we can choose a given solution. This includes problems involving oscillation between generally two possible solutions, a frequent cause of which is the degeneracy of measurements with respect to aerosol loading. Degeneracy is caused by more than one aerosol scene

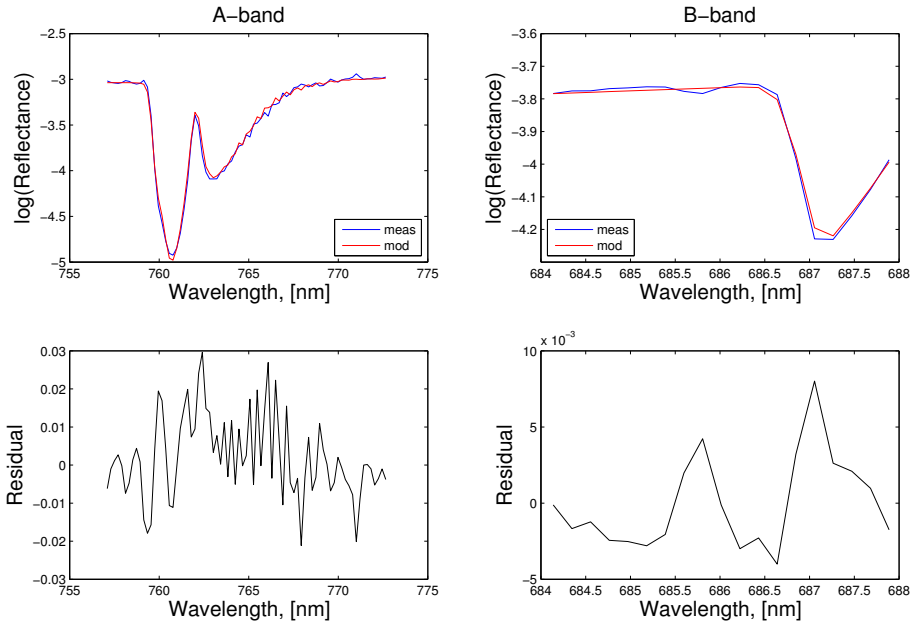

Fig. 8. A fit showing the O_2 A- and B-band spectra simulated by the forward model (red) against the spectra measured by SCIAMACHY(blue), in the upper left and right panels respectively. The log(Reflectance) indicates the natural logarithm of the measured and modeled reflectances. The bottom panels show the corresponding dimensionless residuals $\left(\frac{\log R_{\mathrm{mod}} - \log R_{\mathrm{meas}}}{\log R_{\mathrm{meas}}}\right)$ given here by the difference of the two spectra relative to the measurement.

corresponding to the same reflectance within a given channel. The simultaneous use of the A- and B-bands decreases the probability of occurrence of such oscillations. Additional use of spectrally farther SCIAMACHY measurements can be theoretically expected to ameliorate such oscillations.

Figure 8 shows a typical fit with a SCIAMACHY measurement. The residuals obtained in the oxygen A-band strongly resemble the residuals presented by van Diedenhoven et al. (2005). Moreover, they also resemble the residuals obtained by van Diedenhoven et al. (2007) after retrieving cloud parameters from GOME measurements in the oxygen A-band. As discussed by van Diedenhoven et al. (2007), the fact that similar residuals are obtained using two different instruments and with different retrieval procedures may indicate that many of the residuals result from errors in spectroscopic parameters (Rothman et al., 2005) or the assumed line shapes, or from neglecting collision induced absorption in the forward model (Tran et al., 2006), rather than from errors in the aerosol model.

However, since the quality of our retrievals vary with the scene being observed, we have flagged our retrievals "good", "fair", "oscillating" or "bad". A "good" convergence is said to occur when the model succeeds in arriving at a stable solution for which the modeled reflectance lies within the error bounds of the retrieval. A "fair" retrieval arrives like a "good" retrieval at a stable solution, but the modeled reflectance lies outside the error bounds of the retrieval. The solution can be made unstable by the presence of an oscillation when two competing solutions are present. This is when we select the one with the lower least squares fit and flag the solution "oscillating". In cases where there is neither a stable nor an oscillating solution, the retrieval is flagged as "bad".

The aerosol/cloud optical thicknesses retrieved from SCIAMACHY data are color-coded according to the "goodness" of the fit and plotted against the corresponding relative contrast in the upper panel of Fig. 9, which suggests that the "goodness" of our fit decreases with increasing optical thickness. This is not a surprising result, as scene inhomogeneities are also expected to increase with increasing optical thickness, causing a steady departure of the forward model from reality. The increase in optical thickness also correlates well with the decrease in relative contrast, as hypothesized in Sanghavi et al. (2010). A linear correlation yields a coefficient of $r = -0.788$. The relative contrast at low to intermediate values of aerosol loading show highest sensitivity to changes in viewing geometry, viz. solar and line-of-sight zenith angles and (to a lesser extent) the corresponding azimuth angles, as a result of which the spread in relative contrast is largest there. The conjecture of negative relative contrast corresponding mainly to cloudy or very hazy scenes is also verified from these results.

The bottom panel of Fig. 9 shows the temporal progression of the optical thickness as quantified on the left ordinate as well as the relative contrast depicted on the right ordinate, confirming a good anti-correlation.

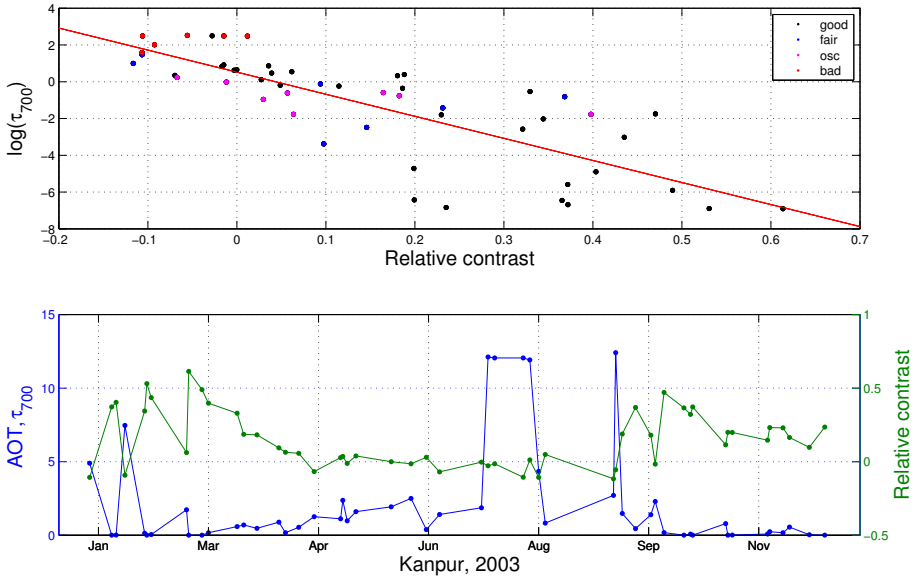

Fig. 9. Upper panel: the natural logarithm of the retrieved AOT plotted against the corresponding relative contrast, calculated as $(\rho_A^a - \rho_B^a)/(\rho_A^a + \rho_B^a)$. The points are color-coded according to the goodness of the retrieval yeilding τ_{700}, with black denoting a good fit, blue denoting fair, magenta representing the presence of oscillation, and red denoting a bad convergence. The red line represents a linear fit of the aerosol optical thickness with respect to relative contrast. The relative contrast and τ_{700} are anti-correlated by a factor of $r = -0.788$. Lower panel: a time series of the retrieved AOT plotted along the left y-axis, and the relative contrast plotted on the right y-axis.

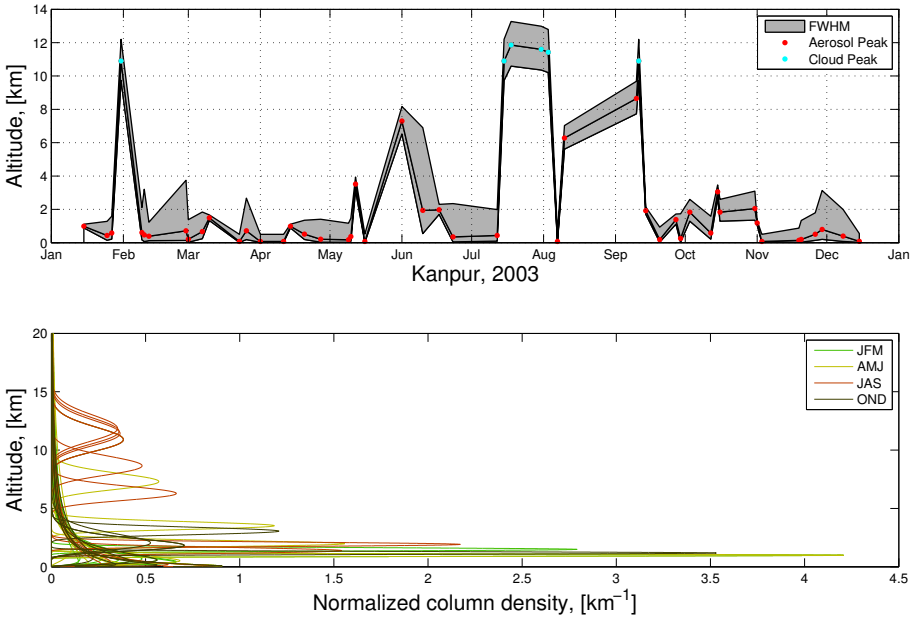

Fig. 10. Upper panel: a time series of retrieved heights of maximum aerosol concentration, represented by red dots for $\tau_{700} <= 5.0$, and cyan dots for $\tau_{700} > 5.0$. The black lines bounding the gray region around the dots represent heights at which the aerosol concentration is half its maximum value. Lower panel: a representation of each lognormal vertical profile retrieved in the case-study over Kanpur. The x-axis may be regarded as the probability density function for the aerosol to be present at a given altitude, hence the unit [km^{-1}]. The retrievals are color-coded by season as shown in the legend. The wet months of July, August and September stand out due to their high altitude profiles, mostly attributable to clouds.

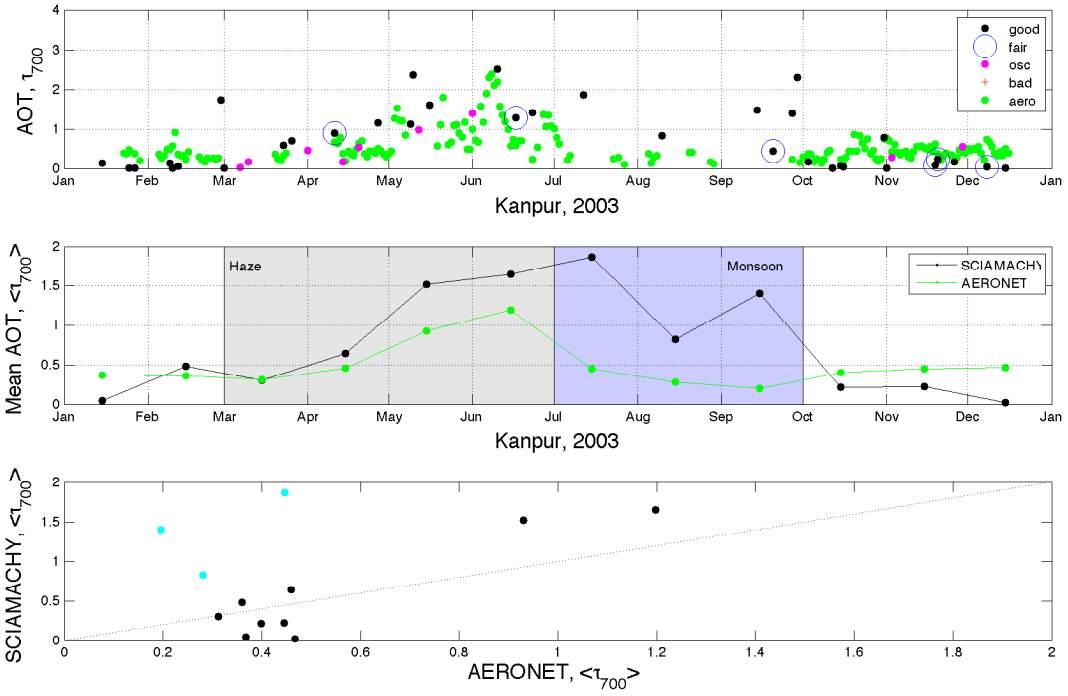

Fig. 11. Top panel: a time series of all AERONET measurements of AOT (675 nm) at Kanpur over the year 2003 (green dots), all SCIAMACHY retrievals of $\tau_{700} <= 4$, color coded according to the goodness of the retrieval. Middle panel: A time progression of the monthly means of both sets of data, AOT measured by AERONET (green) and those retrieved from SCIAMACHY (black dots). Lower panel: a scatter plot of SCIAMACHY monthly means of AOT against AERONET values. Strongly cloud contaminated (SCIAMACHY) data are color-coded cyan. The black line is the 1:1 line. The non-monsoon monthly means show a high correlation coefficient of $r = 0.92$.

The retrieved vertical profiles are shown in Fig. 10, where the upper panel shows a time-progression of the retrieved heights of maximum concentration along with the spread of the aerosol around that height, such that the gray region is bounded by lines corresponding to the heights at which the aerosol concentration falls to half the maximum value. The lower panel shows the form of the resulting vertical distributions. In the upper panel, peak heights corresponding to retrieved optical thicknesses greater than 5 are shown in cyan. It is found that all such cases also correspond to greater elevations, suggesting strongly that these retrievals may correspond to cloudy scenes. The remaining retrievals may correspond to cloudless but also to partially cloudy scenes. The residence of most aerosols over Kanpur between 0–5 km as suggested by these results can be confirmed by comparison with simultaneous twice-daily back-trajectory data (Pickering et al., 2001; Schoeberl and Newman, 1995) available from the AERONET website.

Direct comparison of aerosol optical thickness with AERONET is not possible due to few simultaneous, collocated measurements. However, we have plotted AOT observed by AERONET and SCIAMACHY observations having AOT ≤ 4 as a function of time in the top panel of Fig. 11, assuming other observations to have a greater degree of cloud-contamination. Although AERONET observations greatly outnumber SCIAMACHY retrievals, we can discern a general seasonality, causing the aerosol loading to increase from low values in the months of January–March steadily over the months of April–June, reaching a maximum at the beginning of the rainy monsoon season in mid-June. This is caused mainly due to the seasonal transport of wind-blown dust across the Indo-Gangetic plains (Bhattacharjee et al., 2007). During the monsoon period, which extends from mid-June through the end of September, cloudy scenes become frequent, reflected by decimated AERONET observations and resulting in a presumably high degree of cloud contamination in SCIAMACHY retrievals. The months of October–December see a return of the aerosol loading to the initial "background" values, thus closing an annual cycle.

A comparison of monthly mean data, as shown in the middle and bottom panels of Fig. 11 helps quantify the main differences between SCIAMACHY and AERONET observations. Though a linear correlation between monthly mean AOTs obtained by AERONET and SCIAMACHY yields a high correlation coefficient of $r = 0.92$ for non-monsoon months (January–May, October–December), SCIAMACHY largely underestimates low optical thicknesses, as seen in the periods January–March and October–December. This may be explained by the time-series method used to determine the surface albedo over Kanpur, which cannot correct for

background aerosol that is always present over the given location. As a result, days of comparably low aerosol loading are regarded as almost haze-free by the inversion algorithm due to the "invisibility" of background aerosol in the inversion. Other months, on the other hand, see an overestimation due to cloud contamination that occurs in SCIAMACHY measurements due to the lack of a cloud filter.

As there is no concurrent information on the vertical profile of clouds and aerosols from space-based Lidar in 2003, we cannot yet validate the retrieved aerosol profile. However, the synthetic case study has shown that our approach is conceptually robust.

6 Conclusions

In the work presented in this paper, we have made use of spectra obtained at medium resolution (≈0.4 nm) around the O_2 A- and B-bands of absorption to retrieve aerosol optical depth and the vertical profile of the aerosol using optimal estimation.

Several studies (Heidinger and Stephens, 2010; Wang et al., 2008; Kokhanovsky and Rozanov, 2004; Koelemeijer et al., 2002; Koppers et al., 1997) focus on determining the vertical extent of clouds using the O_2 A-band. Our extension of the measured data in our retrieval to include the weaker O_2 B-band provides, in addition to increased sensitivity to atmospheric layers close to the surface, also the benefit of a different, generally lower, surface albedo for retrievals over land, supplying an additional constraint to our retrieval problem. This results in an ability to quantify not only effective cloud heights for cloudy scenes, but also to retrieve a log-normal approximation of the vertical profile of the aerosol column for hazy scenes. The simultaneous use of the two bands is also critical to removing possible redundancies due to the non-monotonic character of the backscatter reflectance signal with respect to the parameters to be retrieved.

Our method is applicable over both bright and dark surfaces, as long as the bright surface has sufficient contrast between the albedos near the two bands. Fortunately, this is true for most land surfaces (Baldridge et al., 2009). We have demonstrated using Jacobian matrices, information content and error analyses, synthetic sensitivity studies and retrievals using real data that a combined use of the A- and B-band spectra helps remove redundancies while also improving the information content of the inversion problem. Sensitivity studies show a robust retrievability of the AOT and good retrievability of the vertical profile.

We have applied the retrieval to SCIAMACHY observations over Kanpur, India, through the year 2003. Notwithstanding uncertainties in instrumental radiometric calibration and the large footprint of the instrument, we could achieve reasonable agreement with AERONET measurements of optical thickness, with non-monsoon monthly mean aerosol optical thicknesses showing a correlation coefficient of $r = 0.92$. We could obtain a good anti-correlation ($r = 0.788$) between the retrieved optical thickness and the "relative contrast" introduced in Sanghavi et al. (2010). The conjecture of negative relative contrast corresponding mainly to thick clouds was verified.

Currently, large-scale application to SCIAMACHY data is severely challenged by radiometric uncertainties which make a simultaneous retrieval of key aerosol microphysical parameters by using more, spectrally farther-spaced wavelengths practically impossible. However, addressing these issues in future instruments similar to SCIAMACHY, coupled with computational resources and speed-up of the current line-by-line radiative transfer calculations, can allow our approach to be extended to the global scale, especially because it is not restricted to dark surface types.

Acknowledgements. The authors wish to thank three anonymous referees, Bastiaan van Diedenhoven and Luis Guanter for their insightful comments and suggestions, which have greatly contributed to the quality of presentation of our work. The bulk of this work was carried out as part of Suniti Sanghavi's PhD thesis. She would like to express her gratitude to Ulrich Platt for his support and acknowledge the IMPRS for awarding her the scholarship that funded this work.

Edited by: A. Kokhanovsky

References

Aben, I., Hasekamp, O., and Hartmann, W.: Uncertainties in the space-based measurements of CO_2 columns due to scattering in the Earth's atmosphere, J. Quant. Spectrosc. Ra., 104, 450–459, 2007.

Acarreta, J. and Stammes, P.: Calibration comparison between SCIAMACHY and MERIS onboard ENVISAT, IEEE Geosci. Remote Sens. Lett., 2, 31–35, 2005.

Baldridge, A. M., Hook, S. J., Grove, C. I., and Rivera, G.: The ASTER spectral library version 2.0, Remote Sens. Environ., 113, 711–715, 2009.

Balkanski, Y., Jacob, D., Gardner, G., Graustein, W., and Turekian, K.: Transport and Residence Times of Tropospheric Aerosols Inferred from a Global Three-Dimensional Simulation of 210 Pb, J. Geophys. Res., 98, 20573–20586, 1993.

Bhattacharjee, P., Prasad, A., Kafatos, M., and Singh, R.: Influence of a dust storm on carbon monoxide and water vapor over the Indo-Gangetic Plains, Journal of Geophysical Research, 112, D18203, doi:10.1029/2007JD008469, 2007.

Boersma, K. F., Eskes, H. J., and Brinksma, E. J.: Error analysis for tropospheric NO_2 retrieval from space, J. Geophys. Res., 109, D04311, doi:10.1029/2003JD003962, 2004.

Bovensmann, H., Burrows, J., Buchwitz, M., Frerick, J., Noël, S., Rozanov, V., Chance, K., and Goede, A.: SCIAMACHY: Mission objectives and measurement modes, J. Atmos. Sci., 56, 127–150, 1999.

Burrows, J. P., Weber, M., Buchwitz, M., Rozanov, V., Ladstätter-Weißenmayer, A., Richter, A., de Beek, R., Hoogen, R., Bramstedt, K., Eichmann, K.-U., Eisinger, M., and Perner, D.: The

global ozone monitoring experiment (GOME): Mission concept and first scientific results, J. Atmos. Sci., 56, 151–175, 1999.

Callies, J., Corpaccioli, E., Eisinger, M., Hahne, A., and Lefebvre, A.: GOME-2 – Metop's second-generation sensor for operational ozone monitoring, ESA Bull., 102, 28–36, 2000.

Charlson, R., Schwartz, S. E., Hales, J. M., Cess, R., Coakley Jr., J. A., Hansen, J. E., and Hofmann, D. J.: Climate forcing by anthropogenic aerosols, Science, 255, 423–430, 1992.

Charlson, R. J., Langner, J., Rodhe, H., Leovy, C. B., and Warren, S. G.: Perturbation of the northern hemisphere radiative balance by backscattering from anthropogenic sulfate aerosols, Tellus A, 43, 152–163, 1991.

Colarco, P. R., Schoeberl, M. R., Doddridge, B. G., Marufu, L. T., Torres, O., and Welton, E. J.: Transport of smoke from Canadian forest fires to the surface near Washington, DC: Injection height, entrainment, and optical properties, J. Geophys. Res., 109, D06203, doi:10.1029/2003JD004248, 2004.

Corradini, S. and Cervino, M.: Aerosol extinction coefficient profile retrieval in the oxygen A-band considering multiple scattering atmosphere, Test case: SCIAMACHY nadir simulated measurements, J. Quant. Spectrosc. Ra., 97, 354–380, 2006.

Daniel, J., Solomon, S., Miller, H., Langford, A., Portmann, R., and Eubank, C.: Retrieving cloud information from passive measurements of solar radiation absorbed by molecular oxygen and O_2-O_2, J. Geophys. Res., 108, 4515, doi:10.1029/2002JD002994, 2003.

de Graaf, M., Stammes, P., and Aben, E.: Analysis of reflectance spectra of UV-absorbing aerosol scenes measured by SCIAMACHY, J. Geophys. Res., 112, D02206, doi:10.1029/2006JD007249, 2007.

Diner, D., Beckert, J., Reilly, T., Bruegge, C., Conel, J., Kahn, R., Martonchik, J., Ackerman, T., Davies, R., Gerstl, S., Gordon, H. R., Myneni, R., Sellers, P., Pinty, B., and Verstraete, M.: Multi-angle Imaging SpectroRadiometer (MISR) instrument description and experiment overview, Geoscience and Remote Sensing, IEEE T. Geosci. Remote, 36, 1072–1087, 1998.

Dubovik, O., Herman, M., Holdak, A., Lapyonok, T., Tanré, D., Deuzé, J. L., Ducos, F., Sinyuk, A., and Lopatin, A.: Statistically optimized inversion algorithm for enhanced retrieval of aerosol properties from spectral multi-angle polarimetric satellite observations, Atmos. Meas. Tech., 4, 975–1018, doi:10.5194/amt-4-975-2011, 2011.

Guanter, L., Alonso, L., Gómez-Chova, L., Meroni, M., Preusker, R., Fischer, J., and Moreno, J.: Developments for vegetation fluorescence retrieval from spaceborne high-resolution spectrometry in the O_2-A and O_2-B absorption bands, J. Geophys. Res., 115, D19303, doi:10.1029/2009JD013716, 2010.

Heidinger, A. and Stephens, G.: Molecular line absorption in a scattering atmosphere. Part II: Application to remote sensing in the O_2 A band, Journal of the Atmospheric Sciences, 57, 1615–1634, 2010.

Holzer-Popp, T., Schroedter-Homscheidt, M., Breitkreuz, H., Martynenko, D., and Klüser, L.: Improvements of synergetic aerosol retrieval for ENVISAT, Atmos. Chem. Phys., 8, 7651–7672, doi:10.5194/acp-8-7651-2008, 2008.

Houweling, S., Hartmann, W., Aben, I., Schrijver, H., Skidmore, J., Roelofs, G.-J., and Breon, F.-M.: Evidence of systematic errors in SCIAMACHY-observed CO_2 due to aerosols, Atmos. Chem. Phys., 5, 3003–3013, doi:10.5194/acp-5-3003-2005, 2005.

Hunt, G. E. and Grant, I. P.: Discrete space theory of radiative transfer and its application to problems in planetary atmospheres, J. Atmos. Sci., 26, 963–972, 1969.

Koelemeijer, R., Stammes, P., Hovenier, J., and De Haan, J.: Global distributions of effective cloud fraction and cloud top pressure derived from oxygen A band spectra measured by the Global Ozone Monitoring Experiment: comparison to ISCCP data, J. Geophys. Res, 107, 1–9, 2002.

Kokhanovsky, A. and Rozanov, V.: The physical parameterization of the top-of-atmosphere reflection function for a cloudy atmosphere-underlying surface system: the oxygen A-band case study, J. Quant. Spectrosc. Ra., 85, 35–55, 2004.

Kokhanovsky, A. and Rozanov, V.: The determination of dust cloud altitudes from a satellite using hyperspectral measurements in the gaseous absorption band, Int. J. Remote Sens., 31, 2729–2744, 2010.

Kokhanovsky, A., Schreier, M., and von Hoyningen-Huene, W.: The comparison of spectral top-of-atmosphere reflectances measured by AATSR, MERIS, and SCIAMACHY onboard ENVISAT, IEEE Geosci. Remote Sens. Lett., 5, 53–56, 2008.

Koppers, G. A. A., Jansson, J., and Murtagh, D. P.: Aerosal optical thickness retrieval from GOME satellite data in the Oxygen A band, in: Third ERS Symposium on Space at the service of our Environment, ESA SP, European Space Agency, 693–696, 1997.

Kripalani, R. H., Kulkarni, A., Sabade, S. S., Revadekar, J. V., Patwardhan, S. K., and Kulkarni, J. R.: Intra-seasonal oscillations during monsoon 2002 and 2003, Curr. Sci., 87, 325–331, 2004.

Levenberg, K.: A method for the solution of certain problems in least squares, Quart. Appl. Math., 2, 164–168, 1944.

Liu, S. C., McKeen, S. A., and Madronich, S.: Effect of anthropogenic aerosols on biologically active ultraviolet radiation, Geophys. Res. Lett., 18, 2265–2268, 1991.

Lohmann, U. and Feichter, J.: Impact of sulfate aerosols on albedo and lifetime of clouds: A sensitivity study with the ECHAM4 GCM, J. Geophys. Res., 102, 13685, doi:10.1029/97JD00631, 1997.

Marquardt, D.: An algorithm for least-squares estimation of nonlinear parameters, J. Soc. Ind. Appl. Math., 11, 431–441, 1963.

Martonchik, J. V.: Sulphuric acid cloud interpretation of the infrared spectrum of Venus, University of Texas at Austin, 1975.

Menon, S., Hansen, J., Nazarenko, L., and Luo, Y.: Climate effects of black carbon aerosols in China and India, Science, 297, 2250, doi:10.1126/science.1075159, 2002.

Mitchell Jr., J.: The effect of atmospheric aerosols on climate with special reference to temperature near the earth's surface, J. Appl. Meteorol., 10, 703–714, 1971.

Noël, S.: Determination of correction factors for SCIAMACHY radiances and irradiances, Tech. Note IFE-SCIA-SN-20040514, University of Bremen, Bremen, Germany, 2004.

Penning de Vries, M. J. M., Beirle, S., and Wagner, T.: UV Aerosol Indices from SCIAMACHY: introducing the SCattering Index (SCI), Atmos. Chem. Phys., 9, 9555–9567, doi:10.5194/acp-9-9555-2009, 2009.

Phillips, D.: A technique for the numerical solution of certain integral equations of the first kind, J. Assoc. Comput. Mach., 9, 84–97, 1962.

Pickering, K. E., Thompson, A. M., Kim, H., DeCaria, A. J., Pfister, L., Kucsera, T. L., Witte, J. C., Avery, M. A., Blake, D. R., Crawford, J. H., Heikes, B. G., Sachse, G.

W., Sandholm, S. T., and Talbot, R. W.: Trace gas transport and scavenging in PEM-Tropics B South Pacific Convergence Zone convection, Journal of Geophysical Research, 106, 32591, doi:10.1029/2001JD000328, 2001.

Pope III, C.: What Do Epidemiologic Findings Tell Us about Health Effects of Environmental Aerosols?, J. Aerosol Med., 13, 335–354, 2000.

Remer, L., Kaufman, Y., Tanré, D., Mattoo, S., Chu, D., Martins, J., Li, R., Ichoku, C., Levy, R., Kleidman, R., Eck, T., Vermote, E., and Holben, B.: The MODIS Aerosol Algorithm, Products, and Validation, J. Atmos. Sci., 62, 947–973, 2005.

Rodgers, C. D.: Inverse Methods for Atmospheric Sounding: Theory and Practice, World Scientific, Singapore, 2000.

Rothman, L., Jacquemart, D., Barbe, A., Chris Benner, D., Birk, M., Brown, L., Carleer, M., Chackerian, C., Chance, K., Coudert, L., et al.: The HITRAN 2004 molecular spectroscopic database, J. Quant. Spectrosc. Ra., 96, 139–204, 2005.

Rothman, L. S., Gordon, I. E., Barbe, A., Benner, D. C., Bernath, P. F., Birk, M., Boudon, V., Brown, L. R., Campargue, A., Champion, J. P., Chance, K., Coudert, L., Dana, V., Devi, V. M., Fally, S., Flaud, J.-M., Gamache, R. R., Goldman, A., Jacquemart, D., Kleiner, I., Lacome, N., Lafferty, W. J., Mandin, J.-Y., Massie, S. T., Mikhailenko, S. N., Miller, C. E., Moazzen-Ahmadi, N., Naumenko, O., Nikitin, A., Orphal, J., Perevalov, V. I., Perrin, A., Predoi-Cross, A., Rinsland, C. P., Rotger, M., Simeckova, M., Smith, M. A. H., Sung, K., Tashkun, S. A., Tennyson, J., Toth, R. A., Vandaele, A. C., and Vander Auwera, J.: The HITRAN 2008 molecular spectroscopic database, Journal of Quantitative Spectroscopy and Radiative Transfer, 110, 533–572, 2009.

Rozanov, V. and Kokhanovsky, A.: Semianalytical cloud retrieval algorithm as applied to the cloud top altitude and the cloud geometrical thickness determination from top-of-atmosphere reflectance measurements in the oxygen A band, J. Geophys. Res., 109, D05202, doi:10.1029/2003JD004104, 2004.

Salstein, D., Ponte, R., and Cady-Pereira, K.: Uncertainties in atmospheric surface pressure fields from global analyses, J. Geophys. Res, 113, D14107, doi:10.1029/2007JD009531, 2008.

Sanghavi, S., Platt, U., and Landgraf, J.: Bichromatic method for identification of clear-sky scenarios over ground pixel viewed from space, Appl. Optics, 49, 3282–3290, 2010.

Schoeberl, M. and Newman, P.: A multiple-level trajectory analysis of vortex filaments, J. Geophys. Res., 100, 25801, doi:10.1029/95JD02414,1995.

Shannon, C.: The mathematical theory of communication, MD computing, Comput. Med. Pract., 14, 306–317, 1948.

Stammes, P. and Noordhoek, R.: OMI algorithm theoretical basis document volume III: clouds, aerosols, and surface UV irradiance, Tech. rep., Tech. Rep. ATBD-OMI-03, Version 2.0, 2002.

Tikhonov, A.: Solution of incorrectly formulated problems and the regularization method, Dokl. Akad. Nauk SSSR, 151, 501–504, 1963.

Torres, O., Tanskanen, A., Veihelmann, B., Ahn, C., Braak, R., Bhartia, P., Veefkind, P., and Levelt, P.: Aerosols and surface UV products from Ozone Monitoring Instrument observations: An overview, J. Geophys. Res., 112, 1–14, 2007.

Tran, H., Boulet, C., and Hartmann, J.: Line mixing and collision-induced absorption by oxygen in the A band: Laboratory measurements, model, and tools for atmospheric spectra computations, J. Geophys. Res., 111, 15210, doi:10.1029/2005JD006869, 2006.

van Diedenhoven, B., Hasekamp, O. P., and Aben, I.: Surface pressure retrieval from SCIAMACHY measurements in the O_2 A Band: validation of the measurements and sensitivity on aerosols, Atmos. Chem. Phys., 5, 2109–2120, doi:10.5194/acp-5-2109-2005, 2005.

van Diedenhoven, B., Hasekamp, O. P., and Landgraf, J.: Retrieval of cloud parameters from satellite-based reflectance measurements in the ultraviolet and the oxygen A-band, J. Geophys. Res., 112, D15208, doi:10.1029/2006JD008155, 2007.

Veefkind, J. and de Leeuw, G.: A new algorithm to determine the spectral aerosol optical depth from satellite radiometer measurements, J. Aerosol Sci., 29, 1237–1248, 1998.

Veefkind, J., De Leeuw, G., Durkee, P., Russell, P., Hobbs, P., and Livingston, J.: Aerosol optical depth retrieval using ATSR-2 and AVHRR data during TARFOX, J. Geophys. Res., 104, 2253–2260, 1999.

Wang, P., Stammes, P., van der A, R., Pinardi, G., and van Roozendael, M.: FRESCO+: an improved O_2 A-band cloud retrieval algorithm for tropospheric trace gas retrievals, Atmos. Chem. Phys., 8, 6565–6576, doi:10.5194/acp-8-6565-2008, 2008.

Weaver, W.: Recent contributions to the mathematical theory of communication, The Mathematical Theory of Communication, The University of Illinois Press, Urbana, Ill., 1–16, 1949.

Winker, D., Pelon, J., and McCormick, M.: The CALIPSO mission: Spaceborne lidar for observation of aerosols and clouds, in: Proceedings of SPIE, vol. 4893, p. 1, 2003.

Yang, E. S., Biazar, A. P., and Christopher, S. A.: P2.6 CMAQ air quality forecasts using satellite aerosol retrievals, in: Papers from the 88th Annual AMS Meeting, American Meteorological Society, 2008.